

X-ray Spectroscopy Studies of Ligand-protected and Zeolite-confined Silver  
Nanoclusters

by

Ziyi Chen

Submitted in partial fulfilment of the requirements  
for the degree of Master of Science

at

Dalhousie University  
Halifax, Nova Scotia  
August 2020

© Copyright by Ziyi Chen, 2020

## Table of Contents

List of Tables .....	v
List of Figures .....	vi
Abstract .....	ix
List of Abbreviations and Symbols Used .....	x
Acknowledgements .....	xii
Chapter 1 - Introduction .....	1
1.1 Noble Metal Nanoparticles.....	1
1.2 Silver Nanoparticles .....	3
1.3 Silver Nanoclusters .....	5
1.4 Motivation and Structure of Thesis .....	8
Chapter 2 - Experimental Techniques.....	10
2.1 Chemical Synthesis .....	10
2.2 X-ray Absorption Spectroscopy (XAS) .....	12
2.2.1 X-ray Absorption Near Edge Structure (XANES) .....	15
2.2.2 Extended X-ray Absorption Fine Structure (EXAFS).....	17
2.2.3 Theoretical Simulation .....	21
2.3 X-ray Photoelectron Spectroscopy (XPS).....	21
Chapter 3 - Bonding Properties of $[\text{Ag}_{25}(\text{SR})_{18}]^{-}$ Nanocluster by X-ray Spectroscopy ....	24
3.1 Introduction .....	24
3.2 Experimental Methods .....	26
3.2.1 Synthesis of Nanoclusters.....	26
3.2.2 XPS Measurements and Data Analysis .....	26

3.2.3 XAS Measurements and Data Analysis.....	26
3.3 Results and Discussion.....	28
3.3.1 XPS Study of Electronic Properties.....	28
3.3.2 XAS Study of Ag <sub>25</sub> .....	32
3.4 Summary .....	38
Chapter 4 - The Structure and Property of Ag Nanoclusters Confined in Zeolites .....	39
4.1 Introduction .....	39
4.2 Experiment Methods .....	40
4.2.1 Synthesis of Nanoclusters.....	40
4.2.2 TEM Measurements .....	41
4.2.3 XAS Measurements and Data Analysis.....	42
4.2.4 Catalytic Reaction.....	42
4.3 Results and Discussion.....	43
4.3.1 Silver Nanoclusters in Zeolite Y .....	43
4.3.2 Silver Nanoclusters in Zeolite Mordenite.....	49
4.3.3 Comparison of Ag Nanoclusters in Different Zeolites with Same Concentration .....	53
4.3.4 Catalytic Reaction of 1.0 wt% Ag@Zeolite Y .....	56
4.4 Summary .....	57
Chapter 5 - Conclusions and Future Work.....	59
5.1 Conclusions .....	59
5.2 Future work .....	60
References.....	62
Appendix A – Supporting Information for Chapter 3.....	69

Appendix B – Copyright Agreement for Chapter 1 .....	70
Appendix C – Copyright Agreements for Chapter 2 .....	71

## List of Tables

<b>Table 2-1.</b> X-ray absorption edges and their corresponding electronic transitions.....	15
<b>Table 3-1.</b> Multiple-component fitting results of XPS core-level spectra of Ag <sub>25</sub> and Au <sub>25</sub> . .....	28
<b>Table 3-2.</b> Valence band center position and width of 25-atom NCs and foils. ....	32
<b>Table 3-3.</b> Structural parameters of Ag <sub>25</sub> at RT and LT.....	37
<b>Table 4-1.</b> Structural parameters of 1.0 wt% Ag@Zeolite Y and 2.0 wt% Ag@Zeolite Y as obtained from FT-EXAFS fittings. ....	48
<b>Table 4-2.</b> Structural parameters of Ag@MOR as obtained from FT-EXAFS fittings. ..	53
<b>Table 4-3.</b> Structural parameters of 2.0wt% samples as obtained from FT-EXAFS fittings.....	56

## List of Figures

<b>Figure 1-1.</b> a) Fourier-transformed EXAFS spectra with proposed structures. b) MIC values of Cys-Ag and PVP-Ag NPs after 20 h. Reproduced with permission. <sup>23</sup> Copyright 2015 American Chemical Society.....	4
<b>Figure 1-2.</b> Structure of Ag <sub>44</sub> (SR) <sub>30</sub> . Grey: metal core Ag; Blue: staple Ag; Yellow: S. Carbon and hydrogen atoms in ligands are not shown for clarity.....	7
<b>Figure 1-3.</b> Structure of Linde Type A (LTA) zeolite and Ag NCs model confined within zeolite. ....	8
<b>Figure 2-1.</b> Demonstration of a typical XAS spectrum consisting of the XANES and EXAFS regions. ....	14
<b>Figure 2-2.</b> Scheme of typical XAS experiment set-up. ....	14
<b>Figure 2-3.</b> Demonstration of electronic analysis for Pt L <sub>3</sub> -edge of Pt foil and PtO <sub>2</sub> . ....	16
<b>Figure 2-4.</b> a) FT-EXAFS spectrum of Ag foil. b) Simulated FT-EXAFS spectra with increased coordination number. Adapted with permission. <sup>76</sup> Copyright 2014, American Chemical Society. c) Crystal structure models with different sizes and coordination numbers. ....	20
<b>Figure 2-5.</b> a) FT-EXAFS data for tiopronin-protected Ag NCs. b) Wavelet transformations of the EXAFS data for tiopronin-protected Ag NCs. <sup>39</sup> Copy right 2015, American Chemical Society.....	20
<b>Figure 2-6.</b> Scheme of generation and detection of photoelectrons of XPS instrument..	22
<b>Figure 2-7.</b> a) Core-level XPS spectra of Ag foil and Ag <sub>25</sub> NCs. b) Valence band XPS spectra of Au foil and Au <sub>25</sub> NCs. ....	22
<b>Figure 3-1.</b> a) Ag 3d <sub>5/2</sub> XPS spectra of Ag <sub>25</sub> and Ag foil. b) Multiple-component fitting of Ag 3d <sub>5/2</sub> XPS spectrum of Ag <sub>25</sub> .....	28
<b>Figure 3-2.</b> a) Ag 4d XPS spectra of Ag <sub>25</sub> and Ag foil. b) Au 5d XPS spectra of Au <sub>25</sub> and Au foil. ....	31
<b>Figure 3-3.</b> a) Ag K-edge XANES spectra and b) first derivatives of the XANES spectra for Ag foil, experimental data, and averaged simulation of Ag <sub>25</sub> . c) Simulations of XANES spectra and d) first derivatives of the simulated XANES spectra for each site of Ag <sub>25</sub> . ....	33

<b>Figure 3-4.</b> Bond distribution of Ag <sub>25</sub> (SR) <sub>18</sub> and theoretical CNs and bond distances for each shell. Red: S; Light grey: staple Ag; Dark grey: metal core Ag; Blue: distorted staple Ag.....	35
<b>Figure 3-5.</b> a) FT-EXAFS spectra of Ag <sub>25</sub> at two different temperatures and Ag foil. b) Wavelet transformations of the EXAFS data for Ag <sub>25</sub> at room temperature c) Fitting of the FT-EXAFS spectrum of Ag <sub>25</sub> at room temperature. d) Fitting of the FT-EXAFS spectrum of Ag <sub>25</sub> at low temperature (90 K).....	37
<b>Figure 4-1.</b> Schematic illustration of synthesis method for Ag NCs confined within zeolites.....	41
<b>Figure 4-2.</b> Pictures of a) Ag@Zeolite Y solutions and b) Ag@MOR solutions after reduction. The concentration increases from the left to the right.....	41
<b>Figure 4-3.</b> Styrene oxidation reaction with experimental reaction conditions. ....	43
<b>Figure 4-4.</b> TEM images of a) 0.2 wt% b) 0.5 wt% c) 1.0 wt% d)2.0 wt% Ag@Zeolite Y. ....	45
<b>Figure 4-5.</b> a) Ag K-edge XANES spectra of Ag@Zeolite Y samples and foil. b) first derivative spectra of XANES for Ag@Zeolite Y samples and foil. ....	46
<b>Figure 4-6.</b> Ag K-edge FT-EXAFS spectra of four samples and Ag foil. ....	47
<b>Figure 4-7.</b> Fittings of FT-EXAFS spectra of a) 1.0 wt% Ag@Zeolite Y and b) 2.0 wt% Ag@Zeolite Y. ....	48
<b>Figure 4-8.</b> Crystal structures of models with different number of atoms. ....	49
<b>Figure 4-9.</b> TEM images of a) 0.5 wt% Ag@MOR and b) 2.0 wt% Ag@MOR.....	50
<b>Figure 4-10.</b> a) Ag K-edge XANES spectra of Ag@MOR samples and foil. b) first derivative spectra of XANES for Ag@MOR samples and foil. ....	51
<b>Figure 4-11.</b> Ag K-edge FT-EXAFS spectra of Ag@MOR and Ag foil. ....	51
<b>Figure 4-12.</b> Fittings of FT-EXAFS spectra of a) 0.5 wt% Ag@MOR and b) 2.0 wt% Ag@MOR. ....	52
<b>Figure 4-13.</b> a) Ag K-edge XANES and b) first derivative spectra of XANE for samples at 0.5 wt% and foil. c) Ag K-edge XANES and d) first derivative spectra of XANE for samples at 2.0 wt% and foil. ....	54
<b>Figure 4-14.</b> Ag K-edge FT-EXAFS spectra of samples and Ag foil at a) 0.5 wt% and b) 2.0 wt%. Structure of c) mordenite and d) zeolite Y.....	55

**Figure A1.** Crystal structure of  $\text{Ag}_{25}(\text{SR})_{18}$  and  $\text{Au}_{25}(\text{SR})_{18}$  with illustration of their differences and similarity. Carbon and hydrogen atoms in ligands are not shown for clarity..... 69

**Figure A2.** Comparison of the bond distribution of a)  $\text{Ag}_{25}$  and b)  $\text{Au}_{25}$ . ..... 69



## Abstract

Due to the unique structure and properties of silver nanoparticles, they can find applications in a variety of areas such as catalysis, sensing, imaging, and biomedicine. Ultrasmall silver nanoparticles, also known as silver nanoclusters (Ag NCs), are of particular interest because of their ultrahigh surface-to-volume ratio and strong quantum size effect. In this work, the studies of Ag NCs with ligand protection and zeolite confinement are presented. X-ray spectroscopy techniques were employed as a major tool to characterize the structure and electronic properties of these protected Ag NCs.

First, the 25-atom Ag NCs protected with thiolate ligands, Ag<sub>25</sub>, were studied by X-ray photoelectron spectroscopy (XPS) in comparison with its well-studied analogue Au<sub>25</sub>. A unique method was developed to analyze the XPS core-level data of Ag<sub>25</sub> and Au<sub>25</sub>. The results show different charge transfer behavior of Ag atoms in the metal core and ligand shell of the NCs from their Au counterpart. From the XPS valence band results, the d-band width and center position of Ag<sub>25</sub> were also compared with Au<sub>25</sub>. The electronic and structural properties of Ag<sub>25</sub> were further investigated by X-ray absorption spectroscopy (XAS). The quantum simulations of X-ray absorption near-edge structure (XANES) were performed to understand the electronic properties of each site in Ag<sub>25</sub>. It was found that the Ag atoms in the ligand shell have a large impact on the electronic properties of the NCs. In addition, the temperature-dependent bonding property was probed by extended X-ray absorption fine structure (EXAFS). The results suggest that the Ag<sub>25</sub> cluster exhibits more molecular-like behavior than Au<sub>25</sub> as the temperature changes.

Next, Ag NCs protected by a hard template, zeolites, were studied. The atomic structure and electronic properties of Ag NCs were found to be controllable by adjusting the concentration of silver ion precursor and selecting different types of zeolites. The zeolites with 3D channels showed a better ability to confine small Ag NCs within frameworks than zeolites with 2D channels. The Ag K-edge XANES together with its first derivative spectra were found to be useful in distinguishing the different types of surface Ag-O bonds in the NCs. A preliminary study on the catalytic activity of the NCs was further conducted using the styrene oxidation reaction, and their catalytic properties were compared with the results of similar Ag-zeolite catalysts reported in the literature.

Overall, studies on Ag NCs protected by two different types of templates were presented. The site-specific analysis of ligand-protected Ag<sub>25</sub> NCs using X-ray spectroscopy techniques gives an in-depth understanding of the electronic and bonding properties of each representative site in the NCs. These results offer a detailed picture on the structure-property relationship of the NCs, which can provide guidance for their potential applications. The study of Ag NCs confined within zeolites suggests their structure and electronic properties can be tuned by controlling the concentration of silver ion precursor and types of zeolites. A preliminary catalytic study showed that the zeolite-confined NCs prepared in this work exhibit promising catalytic, and implied that these Ag NCs with controllable structure and electronic properties could be promising materials for catalytic applications.

## List of Abbreviations and Symbols Used

APS	Advanced Photon Source
BBU	Basic building unit
BDT	1,3-benzenedithiol
TBHP	Tert-butyl hydroperoxide
CBU	Composite building unit
CN	Coordination number
Cys	Cysteine
DFT	Density functional theory
EXAFS	Extended X-ray absorption fine structure
FT	Fourier-transformation
FWHM	Full width at half maximum
Au NPs	Gold nanoparticles
LTA	Linde Type A
LT	Low temperature
MIC	Minimum inhibitory concentration
MOR	Mordenite
NC	Nanocluster
NP	Nanoparticle
NMR	Nuclear magnetic resonance
Pt NP	Platinum nanoparticle
PVP	Polyvinylpyrrolidone
PEG	Polyethylene glycol
RT	Room temperature
SEM	Scanning electron microscopy
Ag NP	Silver nanoparticle
SERS	Surface-enhanced Raman spectroscopy
SPR	Surface plasmon resonance
TMS	Tetramethylsilane
TEM	Transmission electron microscopy

SG	Thiolate of glutathione
TPP	Triphenylphosphine
WT	Wavelet transform
XAS	X-ray absorption spectroscopy
XANES	X-ray absorption near edge structure
XPS	X-ray photoelectron spectroscopy
$E_0$	Absorption edge energy
$\mu(E)$	Experimental X-ray absorption coefficient
$I_f$	Fluorescence intensity
$I_0$	Incident X-ray intensity
$\mu_0(E)$	Intrinsic X-ray absorption coefficient
$\hbar$	Reduced Plank's constant
$f(k)$	Scattering amplitude
$\delta(k)$	Scattering phase shift
$k$	Wavenumber
wt%	Weight percentage
$\chi(E)$	X-ray absorption fine structure function
$I_t$	X-ray intensity after transmission

## **Acknowledgements**

First, I would like to thank my supervisor, Dr. Peng Zhang, for his support and guidance. Peng helped me start my research and guided me on how to solve scientific problems. I am so grateful for all that he has taught me. I would also like to thank my supervisory committee member Dr. Erin Johnson for reading my thesis and providing advice for my research. I also wish to thank previous and current Zhang group members, especially Paul Duchesne, Andrew Walsh, David Morris, David Do, and Tianjun Zhang. Thanks should also go to beamline scientists (Zou Finfrock, Debora Motta Meria, Tianpin Wu) and collaborators (Dr. Manzhou Zhu, Dr. Nanfeng Zheng). Finally, I would like to thank my friends and my parents for their support and encouragement.

## Chapter 1 - Introduction

### 1.1 Noble Metal Nanoparticles

Nanoparticles (NPs) are particles that have dimensions between 1 and 100 nm.<sup>1</sup> They often show unique properties that are different from their bulk counterparts such as high surface energies, high surface-to-volume ratios, size- and shape-dependent optical properties.<sup>2,3</sup> The properties of NPs can be efficiently tailored by controlling their sizes, shapes, and surfaces. Therefore, NPs have various applications in different fields such as catalysis, biomedicine, and biosensing.<sup>4</sup> Generally, the synthesis of NPs can be categorized into either the bottom-up or the top-down methods.<sup>5</sup> The bottom-up approach involves the reduction of metal ions, where the NPs are formed by the assembly and growth of atoms and molecules step by step; top-down synthesis involves breaking large NPs or bulk materials into small nano-sized particles.<sup>6</sup> The choice of synthesis method is important in controlling the structure and properties of NPs.

Among these nanomaterials, the noble metal NPs have drawn great attention.<sup>7,8</sup> Perhaps the most unique property of noble metal NPs is their optical properties. In 1908, Gustav Mie first reported the surface plasmon resonance (SPR) phenomenon: when the light interacts with metal NPs, it will result in the collective oscillation of conduction electrons within a confined surface.<sup>9</sup> The SPR frequency, which depends on the composition, size, shape, and surrounding medium of NPs, is an important factor that can affect their optical applications. Because of this unique optical property, noble metal NPs (especially Au and Ag NPs) are widely used in bio-applications.<sup>7</sup> For example, negatively charged Au NPs can be used as biosensors to detect DNA.<sup>10</sup> Moreover, some noble metal NPs with SPR located within the near infrared region can be applied for bio-imaging. For

instance, Ag-Au core-shell NPs have been applied to image bacteria, where they showed strong antibacterial activity.<sup>11</sup>

Noble metal NPs also exhibit catalytic properties due to their high surface-to-volume ratios.<sup>8</sup> Their catalytic activities can be improved by tuning their physical and chemical properties. Due to the high surface areas of NPs, the reactants can easily interact with the surface of NPs. Thus, catalytic reaction can occur in mild conditions when using NPs as catalysts. Reducing the sizes of NPs is a promising method to enhance their catalytic performance. When the sizes of NPs are decreased, there will be more uncoordinated surface atoms, which can influence the effectiveness of chemisorption. The sizes of NPs can be controlled by using different metal/ligands concentration ratios.<sup>12</sup> One example is in the work by Suchomel et al., who synthesized Au NPs with diameters from 6 to 22 nm; they found that the smallest NPs can enhance the catalytic activity for the reduction of 4-nitrophenol. Another factor that can modify the surface chemisorption features is the shape of NPs. Different shapes can have specific atomic arrangements, which means that they have different atomic sites on the surfaces. There are many different shapes of NPs such as cubes, spheres, and nanorods. As an example, the tetrahedral Pt NPs showed higher catalytic activity for the reaction between hexacyanoferrate (III) and thiosulfate ions than the cubic and near sphere Pt NPs.<sup>13</sup> The tetrahedral Pt NPs had sharp edges and corners, so more active atoms were presented in tetrahedral Pt NPs than in other shapes.

Moreover, the composition of NPs can also affect their catalytic properties. The electronic properties of metal NPs can be changed upon including other metals in a monometallic system. Consequently, the catalytic properties will be altered. A good

example is bimetallic NPs consisting of Pt and additional metals; PtM (M= Au, Ni, Cu) NPs supported on iron oxide are good catalysts for CO oxidation.<sup>14</sup> They showed better catalytic performance than the monometallic Pt NPs. The bimetallic system can induce the change of Pt d-band, while the adjacent additional metals can have partial charges that cooperate with Pt to enhance its catalytic properties. Therefore, the properties of noble metal NPs can be controlled by tuning their sizes, shapes, and composition.

## **1.2 Silver Nanoparticles**

Among all noble metal NPs, silver NPs are most widely used in many different fields because of their antimicrobial and SPR properties.<sup>15</sup> Before the development of nanotechnology, silver had already been in use for a long time. As early as 1000 B.C., silver was used to make water containers to keep water fresh.<sup>16</sup> Silver compounds, such as silver nitrate, were applied in the treatment of disease and infection.<sup>17</sup> However, the Ag-based compounds are toxic to microorganisms.<sup>18</sup> One effective way to make them micro-compatible is to reduce their sizes. Thus, Ag NPs can overcome the limitation of size. The applications of Ag NPs can be traced back a long time ago. A good example is the Lycurgus cup.<sup>19</sup> The color of this cup can change when the light is shone from different sides. This unique phenomenon can be explained by the SPR properties of Ag NPs. Therefore, Ag NPs are good materials for many applications because of their unique optical, electronic, and antimicrobial properties.

With the development of nanotechnology, Ag NPs have been applied in various fields. Many commercial products contain Ag NPs such as textiles, health supplements, cosmetics, and water filters.<sup>20</sup> Given the good antibacterial properties of Ag NPs, they have many biomedical applications. They can be used as a coating on medical devices to

prevent infection and contamination.<sup>21</sup> Ag NPs have been considered as promising antibacterial agents because they have broad antibacterial activities against different bacteria and they feature low resistance from bacteria.<sup>22</sup> Padoms et al. found that poly(vinylpyrrolidone) (PVP) protected Ag NPs (PVP-Ag) showed better antibacterial activity than cysteine protected Ag NPs (Cys-Ag).<sup>23</sup> Their antibacterial activities are related to the ability to release Ag ions from Ag NPs, which can be affected by their surface structure. As shown in **Figure 1-1**, the Ag<sub>2</sub>S-like surface structures in Cys-Ag can inhibit the dissolution of Ag ions, which cause a higher minimum inhibitory concentration (MIC) values for Cys-Ag.

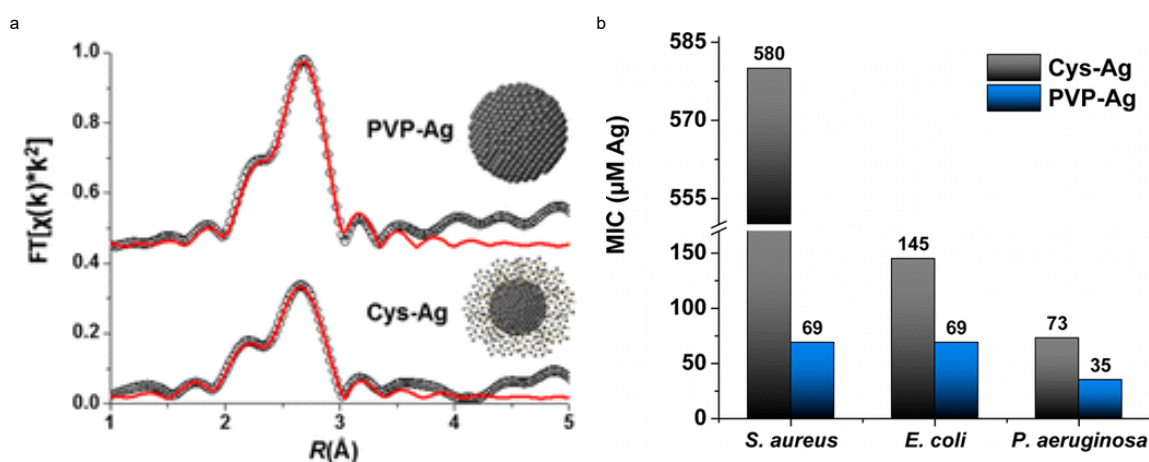


**Figure 1-1.** a) Fourier-transformed EXAFS spectra with proposed structures. b) MIC values of Cys-Ag and PVP-Ag NPs after 20 h. Reproduced with permission.<sup>23</sup> Copyright 2015 American Chemical Society.

Besides their biomedical applications, Ag NPs can also be used as optical labels, sensors, and substrates for surface-enhanced Raman spectroscopy (SERS) because of their SPR optical properties.<sup>24-26</sup> For instance, Ag NPs can enhance the SERS effect on graphene foam, and the sensitivity of the sensor can be modified by controlling the size of the Ag NPs.<sup>27</sup> Therefore, the Ag NPs-decorated sensors can detect chemicals with low concentrations.



Another important application of Ag NPs is in catalysis. The high surface-to-volume ratio of Ag NPs makes them suitable for catalytic applications because they have more surface atoms and active sites than bulk materials. Ag NPs play an important role in organic dye degradation, and many redox reactions such as in the reduction of nitro compounds to amino compounds, and oxidation of olefin.<sup>28,29</sup> As an example, Ag NPs stabilized by alginate fibers can reduce 4-nitrophenol to 4-aminophenol.<sup>30</sup> Ag NPs have also been applied as catalysts for the oxidation of olefin to synthesize industrial products,<sup>31</sup> while the shape of Ag NPs can affect their catalytic activity for the oxidation of styrene reaction.<sup>32</sup> In addition, the Ag NPs catalyst can be easily recovered and reused for many cycles.

### **1.3 Silver Nanoclusters**

Ultrasml NPs are called nanoclusters (NCs). Typically, they have about ten to a few hundred atoms and their diameters are less than 2 nm.<sup>33</sup> These NCs have unique physical and chemical properties.<sup>34</sup> As the size decreases, the quantum confinement effects are induced. The band structure is broken down into discrete electronic structures, which is similar to the energy structure of molecules. Therefore, these NCs have molecule-like properties and they fulfill the gap between metal atoms and NPs.<sup>35</sup> With the decrease in size, the percentage of surface atoms increases. Thus, the surface structure plays an important role in their atomic packing and properties.<sup>36</sup> Bare Ag NCs are not stable, so appropriate protections are needed for these NCs. Generally, these NCs can be stabilized by ligands that have high affinity to Ag or Ag<sup>+</sup>. A good example of stabilizers is the polymers containing carboxylic acid groups such as poly(methacrylic acid).<sup>37,38</sup> Thiol-containing molecules such as glutathione and tiopronin are widely used as

stabilizers for Ag NCs due to the strong interaction between S and Ag.<sup>39-41</sup> Introducing phosphine ligands into pure thiolated NCs can help improve their stability. For instance, Ag<sub>29</sub> NCs protected by pure 1,3-benzenedithiol (BDT) are not stable, but the addition of the triphenylphosphine (TPP) ligand to form [Ag<sub>29</sub>(BDT)<sub>12</sub>(TPP)<sub>4</sub>]<sup>3-</sup> can improve the stability and synthetic yield.<sup>42</sup> This protection method can be considered as using soft templates, which do not have rigid structures. These protecting ligands act as structure directing agents.<sup>43</sup> Another way to protect Ag NCs is to use hard templates, which have rigid structures. For example, dendrimers are good templates to prepare Ag NCs because their terminal groups can bind with Ag ions.<sup>44</sup> The pore structure in dendrimers can encapsulate the reduced Ag metal NCs. Similarly, zeolites have well-defined porous structures, which can confine small metal NCs inside. Therefore, there are two ways to protect Ag NCs: ligand protection (soft-template) and hard-template protection. This work will focus on thiolate-protected and zeolite-confined Ag NCs.

Thiolate-protected metal NCs typically have a metal core with diameters less than 2 nm.<sup>45</sup> Among these ultrasmall NCs, Au NCs have been studied widely due to their good stability. In contrast, the limitation in studying of Ag NCs is their low stability. Recently, Ag NCs are of interest because of their unique physicochemical properties and antibacterial activities.<sup>45</sup> They also have brighter fluorescence than Au NCs in solutions.<sup>46</sup> Generally, Ag NCs have uniform size distributions, and are atomically precise, which can be denoted by their exact formula such as Ag<sub>n</sub>(SR)<sub>m</sub>.<sup>47</sup> Their structure consists of a metal core surrounded by staple motifs. As shown in **Figure 1-2**, Ag<sub>44</sub>(SR)<sub>30</sub> NCs have a Ag<sub>32</sub> metal core and six Ag<sub>2</sub>S<sub>5</sub> staple motifs. The electronic properties of these ligand-protected NCs can be explained by the superatom model.<sup>48,49</sup> The valence electrons in the

metal core of the NCs can be transferred to the protecting ligands. Some of them can have closed shell electron configurations like noble gases. The shell-closing electron count  $n^*$  for  $[\text{Ag}_n(\text{SR})_m]^{-q}$  can be calculated by the following equation:

$$n^* = n_{\text{Ag}}v - m - q \quad (1)$$

where  $v$  equals 1 for the valence of Ag ( $5s^1$ ),  $n_{\text{Ag}}$  is the number of Ag atoms in the metal core,  $m$  is the number of anionic thiolate ligands and  $q$  is the overall charge of the cluster. Therefore, thiolate-protected Ag NCs have high stability if they satisfy the closed shell electron configuration (i.e.  $n^*=2,8,18,\dots$ ). For  $[\text{Ag}_{25}(\text{SR})_{18}]^{-}$ , the electron count is  $n^*=25-18-(-1)$ , which is 8 electrons. Because of the unique properties of thiolate-protected Ag NCs and the biological properties of Ag, they can be used in biomedical applications such as antimicrobial agents, biosensing, and bioimaging.<sup>40,50,51</sup>

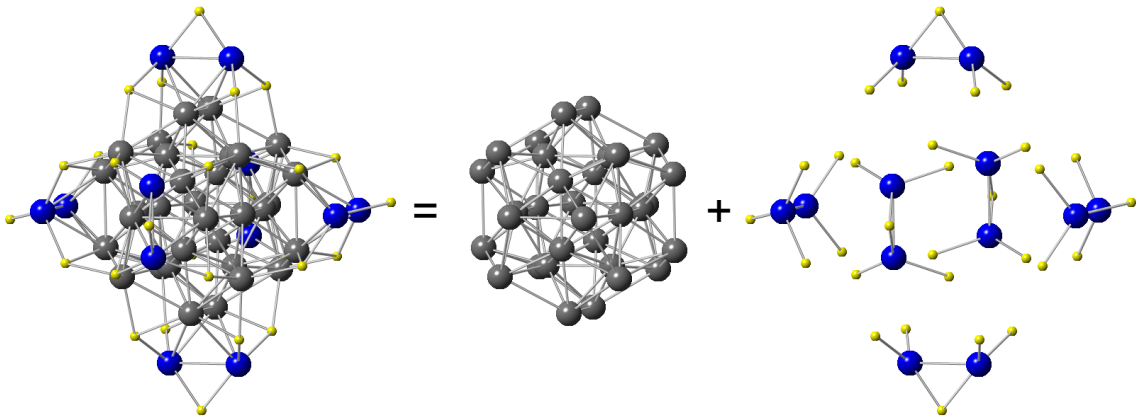


**Figure 1-2.** Structure of  $\text{Ag}_{44}(\text{SR})_{30}$ . Grey: metal core Ag; Blue: staple Ag; Yellow: S. Carbon and hydrogen atoms in ligands are not shown for clarity.

Materials with porous cage structure are considered to be good stabilizers for Ag NPs. Examples include zeolites, which are hard templates that are built up by repeating patterns of basic building units (BBUs), and  $\text{TO}_4$  ( $\text{T}=\text{Si}, \text{Al}\dots$ ), which has tetrahedral geometry.<sup>52</sup> These BBUs are linked by apical oxygen to form composite building units

(CBUs). The basic structure of CBUs is a ring, which can be used to build up the next level structure (larger CBUs). Diverse pores structures can be obtained, such as cages, channels, and cavities. For example, as shown in **Figure 1-3**, three CBUs can form a 3-dimensional alpha cage of Linde Type A (LTA). These structural features are good sites for confining Ag NCs. The molar ratio of Si/Al is an important factor in modifying the structures and properties of zeolites.<sup>53</sup> Various synthesis methods of zeolites has been developed and many different zeolites are commercially available. Since the pore sizes are different, the size of NCs can be controlled by choosing zeolites with appropriate pore sizes.

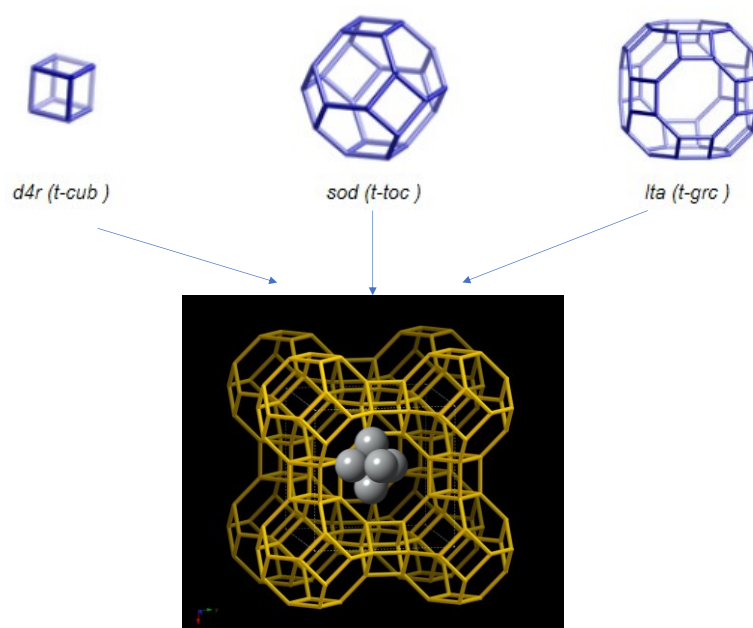


**Figure 1-3.** Structure of Linde Type A (LTA) zeolite and Ag NCs model confined within zeolite.

#### 1.4 Motivation and Structure of Thesis

The goal of this work is to provide an in-depth understanding of the local structure and electronic properties of Ag NCs protected by ligands and zeolites, which can help in designing Ag-based functional nanomaterials for catalytic applications.

Following the introduction, Chapter 2 introduces the experimental techniques that were used in this work. First, the synthesis of Ag NPs and NCs are discussed. Next, the general background information about X-ray absorption spectroscopy (XAS) is given. Then, a detailed discussion about X-ray absorption near edge structure (XANES) and extended X-ray absorption fine structure (EXAFS) is presented. Finally, another X-ray technique, X-ray photoelectron spectroscopy (XPS), is introduced.

Chapter 3 consists of the study of thiolate-protected Ag NCs, specifically Ag<sub>25</sub>. The structural and electronic properties were investigated using XPS and XAS. A close comparison between the electronic properties of Ag<sub>25</sub> and Au<sub>25</sub> is included. The temperature-dependent bonding property was determined. The influence of surface structure on their properties is also discussed from a site-specific perspective.

The study of Ag NCs confined within zeolites is shown in Chapter 4. Ag NCs were prepared with varying concentrations of the silver precursor and different types of zeolites. They were characterized using transmission electron microscopy (TEM) and XAS to probe their structural and electronic properties. The relationship between properties and synthetic factors was determined based on the results of XANES and EXAFS. The results of a preliminary study on their catalytic activity was reported.

Finally, Chapter 5 includes the overall conclusion and future work.

## Chapter 2 - Experimental Techniques

Section 2.2 are reproduced in part with permission from: Zhang, T.; Chen, Z.; Walsh, A. G.; Li, Y.; Zhang, P. Single-atom catalysts supported by crystalline porous materials: views from the inside. *Advanced Materials*. **2020**, *32*, 2002910. Copyright 2020, Wiley-VCH

### 2.1 Chemical Synthesis

Several approaches to Ag NPs synthesis have been developed, including wet chemical, physical, photochemical, and biological methods. Generally, the Ag NPs are produced in solutions with mild conditions in wet chemical approaches. Chemical reduction is the most common way to synthesize Ag NPs.<sup>15</sup> The metal precursors are reduced by organic and/or inorganic reducing agents such as sodium borohydride or sodium citrate. The properties of synthesised Ag NPs depend on factors such as their sizes, shapes, and structures, which can be tuned during the synthesis process. Moreover, the narrow size distribution is important for the stability of NPs. The formation of Ag NPs can be controlled by adjusting synthetic factors such as reducing agents, protecting groups, precursors, reaction temperature, and pH. For example, the Ag NPs size can vary from 2.5 to 7.1 nm in diameter when different silver phosphene precursors were used.<sup>54</sup> Polymeric compounds are widely used as capping ligands of Ag NPs. As an example, poly(ethylene glycol) (PEG) can function as both reducing agent and stabilizer.<sup>55</sup> The chain length can affect the formation of Ag NPs. They also found the shape of NPs can change with the increasing of reaction temperature. Wet chemical approaches do have drawbacks, however, as chemical reducing agents are toxic to the environment. Recently, biological methods have been applied to synthesize Ag NPs by using naturally reducing agents.<sup>56</sup> Bio-organisms can be involved in the synthesis of Ag NPs. A rapid synthesis method of Ag NPs using culture supernatants of bacteria was reported.<sup>57</sup> The culture

supernatants can reduce the  $\text{Ag}^+$  to metallic Ag. By using biosynthesis methods, Ag NPs can be more biocompatible. Ultrasmall bare Ag NCs are even more unstable than bare Ag NPs and they tend to aggregate to form large particles due to their ultrahigh surface energy. So, the protection of Ag NCs needs to be involved in the synthesis. Template synthesis is an effective method to synthesize Ag NCs with protection.<sup>58</sup> There are two possible ways to protect NCs. One is using ligands whose terminal groups have affinity to Ag, which can be considered as soft template synthesis. The other one is using hard templates to encapsulate Ag NCs.

Thiolates are good stabilizers of ultrasmall Ag NCs because of their high affinity to Ag. The size, surface, and structure of thiolate-protected NCs can affect their properties and applications. Thus, the synthesis methods are important because these factors can be controlled during synthesis processes. Unlike Au NCs, the synthesis of Ag NCs is more challenging due to their poor stability.<sup>59</sup> The study of Ag NCs has learned from Au NCs. There are only a few examples of Ag NCs synthesized by the top-down method as this method is more time consuming and the yields of Ag NCs are low. A good example of top-down synthesis method is the formation of  $\text{Ag}_{38}$  NCs from citrate protected Ag NPs.<sup>60</sup> There are many different methods to achieve bottom-up synthesis of Ag NCs such as high temperature route, solid state route and other solution phase methods. For example, Pradeep et al. synthesized  $\text{Ag}_{75}$  by a high temperature route. The synthesis was carried out at 70 °C, so the synthesized NCs have good stability at a high temperature.<sup>61</sup> For the solid-state route, the NCs are obtained by mixing solid metal precursors and ligand, and then followed by reduction with solid  $\text{NaBH}_4$ .  $\text{Ag}_{152}(\text{SR})_{60}$  and  $\text{Ag}_{32}(\text{SG})_{19}$  (SG: thiolate of glutathione) are two good examples of Ag NCs synthesized

by solid state route.<sup>62,63</sup> Recently, the most commonly used method is the solution phase method. The metal precursors and ligands are mixed and then they are reduced by NaBH<sub>4</sub>. The atomically precise NCs, Ag<sub>25</sub>(SR)<sub>18</sub> and Ag<sub>44</sub>(SR)<sub>30</sub>, are synthesized through the solution phase method.<sup>47,64</sup>

Zeolite is a good hard template for Ag NCs, which has well-defined porous structure. Many different methods are available to encapsulate metal NCs into zeolites such as post-synthesis encapsulation methods, and in situ encapsulation method.<sup>65</sup> The post-synthesis encapsulation methods involve ion-exchange, and impregnation, which can introduce metal ions into zeolite frameworks after the synthesis process of zeolites.<sup>66</sup> For in situ encapsulation method, the metal NCs can be introduced during the crystallization process of zeolites. In this work, the ion-exchange method was used to synthesize Ag NCs confined in zeolites. In general, zeolites frameworks possess negative charges, so metal cations occupy the extra-framework sites such as channels and cages to achieve charge balance.<sup>67,68</sup> Silver ions can be introduced into zeolites by ion-exchange process due to the high ion-exchange ability of zeolites, then the Ag NCs can be formed followed by reduction.<sup>69</sup> In this way, most Ag particles should be well distributed inside zeolites with ultrasmall size.

## **2.2 X-ray Absorption Spectroscopy (XAS)**

XAS is a powerful X-ray technique used to study the local structure and the electronic properties of materials. The X-ray source is generated by synchrotron radiation. Synchrotron radiation is emitted as a by-product when the electrons with high speed are accelerated in a circular motion under the effect of a magnetic field.<sup>70</sup> This radiation provides intense photon flux and its wavelength can be tuned from infrared to



hard X-ray.<sup>71</sup> At a synchrotron facility, different beamline stations are designed for specific experiments. In this work, the measurements of XAS were collected at the Sector 20 beamline in the Advanced Photon Source (APS). This synchrotron facility operates at 7.0 GeV. The Sector 20 beamline can collect measurements at an energy range of 2.7 to 35 keV. The monochromator Si (111) was used for energy selection. In this study, the energy was tuned for Ag K-edge measurements (25.514 eV).

XAS measurements are sensitive to dilute samples and the samples do not have to be crystallized or further purified.<sup>72</sup> Typically, there are two regions in an XAS spectrum as shown in **Figure 2-1**: extended X-ray absorption fine structure (EXAFS) and X-ray absorption near edge structure (XANES).<sup>73</sup> As the energy of the X-ray increases and matches that of the electronic transition energy of core electrons, an absorption edge appears in the XAS spectrum. The EXAFS region starts at roughly 50 eV above the absorption edge, with its peaks results from the scattering between absorbing and neighboring atoms.

The signals can be detected in different modes such as fluorescence mode or transmission mode, but fluorescence mode is the most suitable one for dilute samples.<sup>74</sup> The typical experimental set-up scheme is shown in **Figure 2-2**. In this work, all samples were measured by fluorescence mode. The XAS measurements for samples and their references can be measured simultaneously, which is helpful for both energy calibration and data analysis. In transmission mode, the incident X-ray ( $I_0$ ) can be absorbed by samples and reduced to  $I_t$ . The absorption coefficient ( $\mu(E)$ ) equals  $\ln(I_0/I_t)$ . When the signals are collected in fluorescence mode, the electrons in higher energy level can fill the

core hole and release energies after excitation, which can be detected by fluorescence detector ( $I_f$ ). Then, the absorption coefficient is related to the ratio of  $I_f/I_0$ .

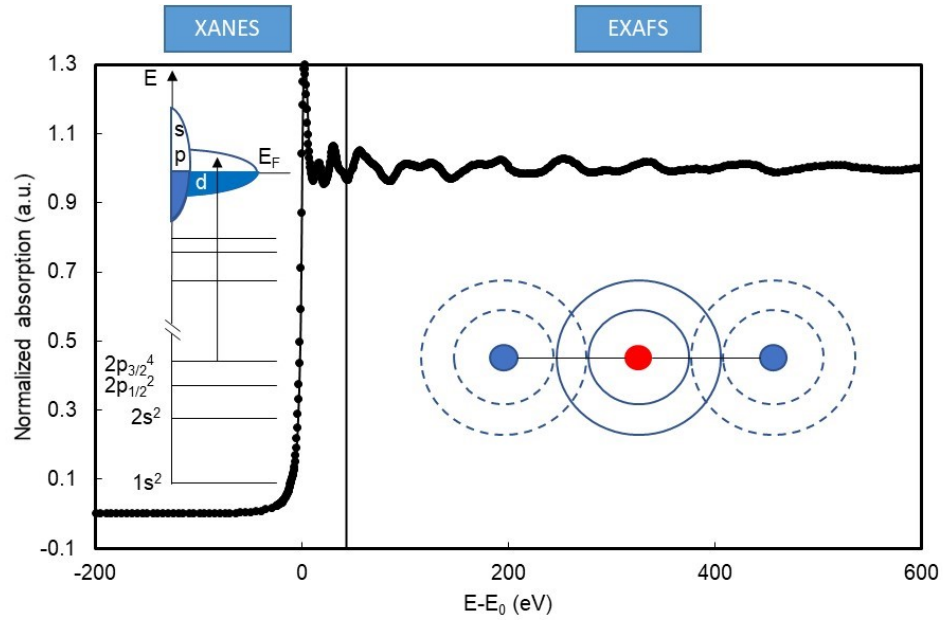


**Figure 2-1.** Demonstration of a typical XAS spectrum consisting of the XANES and EXAFS regions.

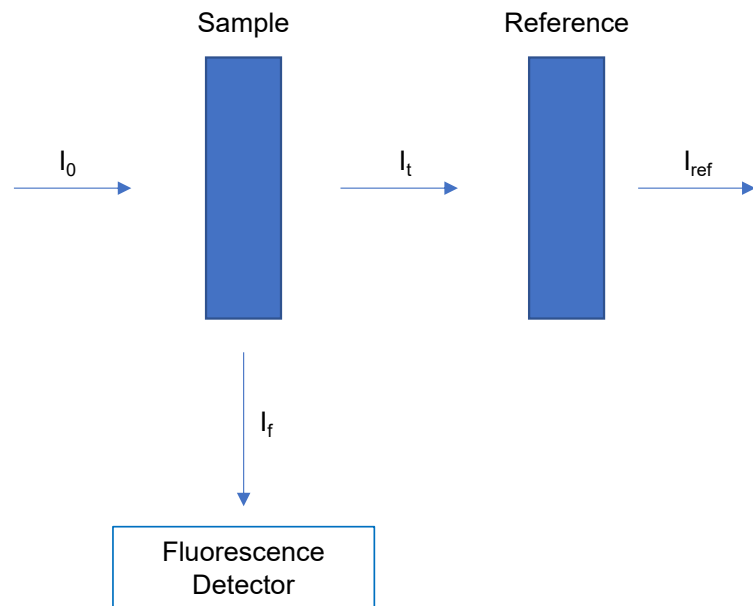


**Figure 2-2.** Scheme of typical XAS experiment set-up.

### 2.2.1 X-ray Absorption Near Edge Structure (XANES)

XAS can be used to characterize the electronic structure of materials, which could then be related to their catalytic activities. In the XAS spectrum, when the X-ray energy matches the energy required for electronic transitions from the core-level to unoccupied states, the absorption edge appears; each element has unique absorption edge energy, so this technique is element sensitive. In XAS, the transitions are satisfied by the dipole selection rule:

$$\Delta l = \pm 1 \quad (2)$$

where  $\Delta l$  is the difference of angular momentum quantum number of initial and final states. The nomenclature of absorption edges and their corresponding electronic transitions are listed in **Table 2-1**.

**Table 2-1.** X-ray absorption edges and their corresponding electronic transitions.

Edge	Electronic transitions
K-edge	1s $\rightarrow$ p
L <sub>1</sub> -edge	2s $\rightarrow$ p
L <sub>2</sub> -edge	2p <sub>1/2</sub> $\rightarrow$ s, d
L <sub>3</sub> -edge	2p <sub>3/2</sub> $\rightarrow$ s, d
M <sub>1</sub> -edge	3s $\rightarrow$ p
M <sub>2</sub> -edge	3p <sub>1/2</sub> $\rightarrow$ s, d
M <sub>3</sub> -edge	3p <sub>3/2</sub> $\rightarrow$ s, d

Since the transitions occur from the core-level to unoccupied valence states, the XANES region can be used to analyze the electronic properties of materials such as oxidation states. As an example, a comparison of the L<sub>3</sub>-edge XANES spectra of Pt and PtO<sub>2</sub> (a 5d transition metal) is shown in **Figure 2-3**. The first spectral feature following the absorption edge (also called the white line) is originated from the Pt occupied 2p to unoccupied 5d state and it is more intense for PtO<sub>2</sub> (+4 oxidation state) than for Pt foil (0

oxidation state) due to the less occupied 5d state in PtO<sub>2</sub>. Therefore, a more intense white line appears in the XANES spectrum if the absorbing atom contains more positive charge. The oxidation states of unknown compounds can be estimated when compared to carefully chosen references with known oxidation states. Furthermore, as the oxidation states change, the absorption energy shifts. Absorbing atoms at higher oxidation states require more energy to excite the core-level electrons, so the absorption edge will shift positively. Practically, the absorption edge shift can be determined using its first derivative peak position. In order to probe the different oxidation states and the amount of each species in a sample, XANES can also be analyzed quantitatively using linear combination fitting.<sup>75</sup> Thus, the electronic properties of samples can be studied based on intensity of the first peak, the shift of the absorption edge and linear combination analysis of the XANES region.

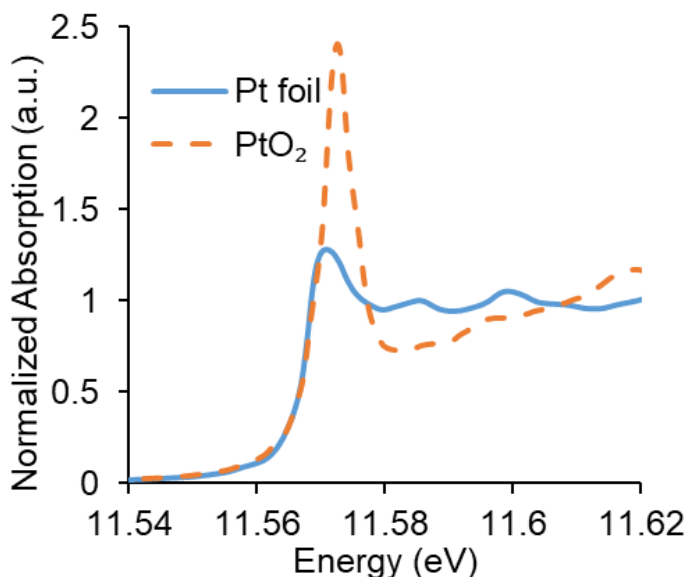


**Figure 2-3.** Demonstration of electronic analysis for Pt L<sub>3</sub>-edge of Pt foil and PtO<sub>2</sub>.

### 2.2.2 Extended X-ray Absorption Fine Structure (EXAFS)

After excitation of core electrons, a photoelectron wave is produced, which interacts with the neighboring atoms. This interaction can cause the photoelectron wave to scatter back to the original absorbing atom. The amplitude and phase of the resulting wave depends on the incident photon energy and atomic number of backscattering atoms. The oscillations in EXAFS are the results of in-phase or out-of-phase from photoelectron waves. Hence, EXAFS contains information about the local structure of absorbing and neighboring atoms such as coordination numbers (CNs), bond distances and local disorder. In order to extract the structural information, the fine structure  $\chi(E)$  must be isolated by using the following equation:

$$\chi(E) = \frac{\mu(E) - \mu_0(E)}{\Delta\mu_0(E)} \quad (3)$$

The smooth background of absorptions for isolated atom,  $\mu_0(E)$ , is subtracted from the actual absorption coefficient,  $\mu(E)$ , and then divided by the difference in intensity before and after the edge,  $\Delta\mu_0(E)$ . This process can help remove the background and normalize the data. Then, the fine structure  $\chi(E)$  can be expressed in terms of photoelectron wavenumber,  $k$ :

$$k = \sqrt{\frac{2m(E - E_0)}{\hbar^2}} \quad (4)$$

where  $m$  is the mass of electron,  $E$  the energy of incoming X-ray,  $E_0$  the energy of absorption edge, and  $\hbar$  the reduced Plank constant. The resulting plot is referred as  $\chi(k)$ , or  $k$ -space. Typically, the  $k$ -space needs to be weighted by  $k^2$  or  $k^3$  to account for the decay of oscillation at high  $k$  region. Then, the  $k$ -space can be transformed to pseudo

radical function (R) space using the Fourier-transformation, denoted as FT-EXAFS.<sup>76</sup> By fitting the FT-EXAFS data, the CNs of absorbers and bond distances between the absorbing and neighboring atoms can be obtained based on the following equation:

$$\chi(k) = \sum_j \frac{S_0^2 N_j e^{-2k^2 \sigma_j^2} e^{-2R_j/e^{\lambda(k)}} f_j(k)}{k R_j^2} \sin(2k R_j + \delta_j(k)) \quad (5)$$

where  $f(k)$  and  $\delta(k)$  are the photoelectron scattering amplitude and phase shift of the neighboring atom, respectively.  $S_0^2$  is the amplitude reduction factor, which typically can be obtained from foil reference. If  $f(k)$  and  $\delta(k)$  are known, a distance to neighboring atom (R), coordination number (N), and mean-square disorder of neighbor distance ( $\sigma^2$ ) can be determined. Moreover,  $j$  represents a coordination shell or scattering path.

A typical FT-EXAFS spectrum of Ag foil is shown in **Figure 2-4a**. Each peak in the FT-EXAFS spectrum corresponds to different scattering between atoms, which corresponds to either different types of bonds or the same type of bonds with varied length. The intense peaks within 1-3 Å are typically the most interesting features: peaks below or around 2 Å correspond to bonding between metal atoms and lighter elements such as oxygen, nitrogen, and sulfur; peaks between 2 and 3 Å correspond to metal-metal bonds. The features above 3 Å can be due to either multiple scatterings or longer distance scatterings of atomic pairs.<sup>77</sup> In the FT-EXAFS spectrum, the peak intensity is positively related to CNs (**Figure 2-4b**): peaks with higher intensity are shown to correspond to higher CNs. As the size of the clusters increases as shown in **Figure 2-4c**, the average CN increases. From the CNs obtained by fitting the EXAFs data, the size of the metal NCs and the local structure of atoms in the samples can be inferred. Hence, the

information from EXAFS can be used to probe the local coordination environments of metals and to help propose potential structure models.

There is a new technique for XAS data analysis, called wavelet transform (WT). As mentioned previously, the data process of EXAFS requires Fourier transform. FT-EXAFS can show a qualitative estimation of radical distance distribution. However, FT-EXAFS has limitations. For example, it cannot distinguish different types of scattering paths with the same bond lengths.<sup>78</sup> WT provides a complementary method to FT-EXAFS by combining radical distance distribution and k-space in the form of a 2D-contour plot, where the k-space shows the oscillation caused by a target atom and backscattering atoms.<sup>39,79,80</sup> As an example, **Figure 2-5a** and **b** show the FT-EXAFS and WT-EXAFS of silver NCs protected by tiopronin.<sup>39</sup> In the FT-EXAFS spectrum, only two scattering paths were assigned corresponding to Ag-S and Ag-Ag shells, while the peak above 3 Å could not be identified. However, in the WT-EXAFS plot, the peak at around 3.3 Å was able to be assigned as another Ag-Ag shell (since the k value of this peak was the same as the first Ag-Ag shell). Therefore, WT-EXAFS is a good tool to help with the assignment of scattering paths that could be missed from EXAFS analyses.

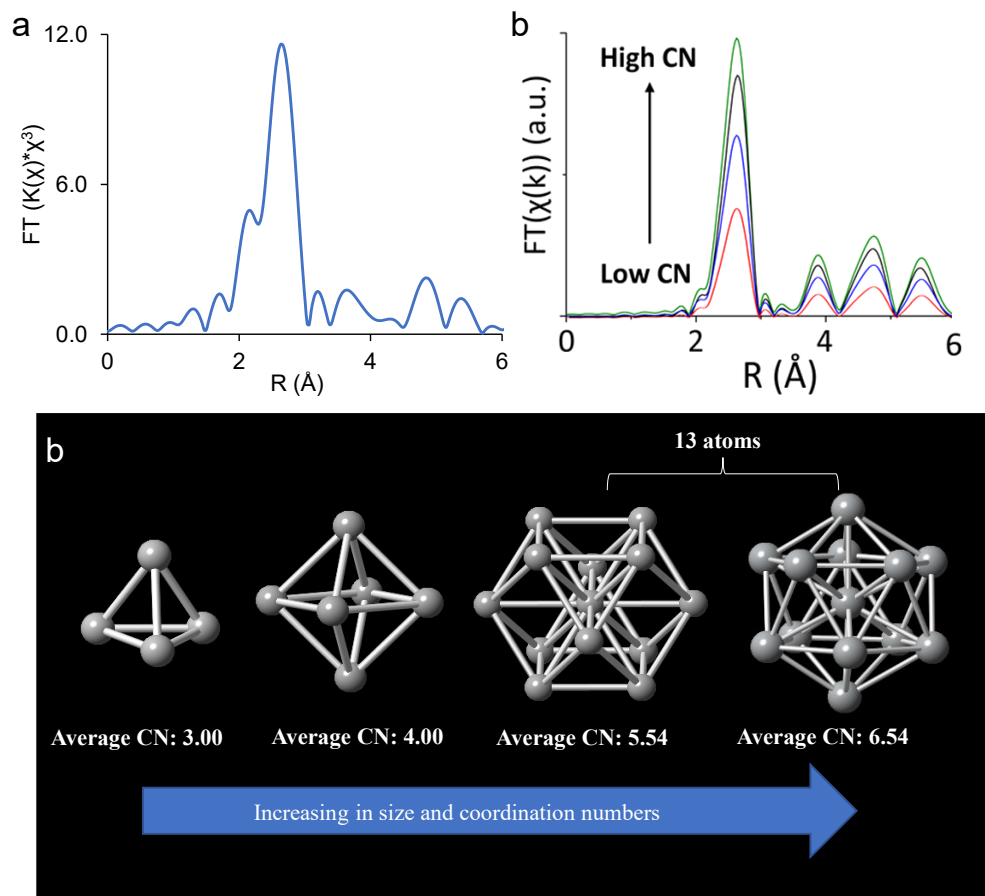


**Figure 2-4.** a) FT-EXAFS spectrum of Ag foil. b) Simulated FT-EXAFS spectra with increased coordination number. Adapted with permission.<sup>76</sup> Copyright 2014, American Chemical Society. c) Crystal structure models with different sizes and coordination numbers.

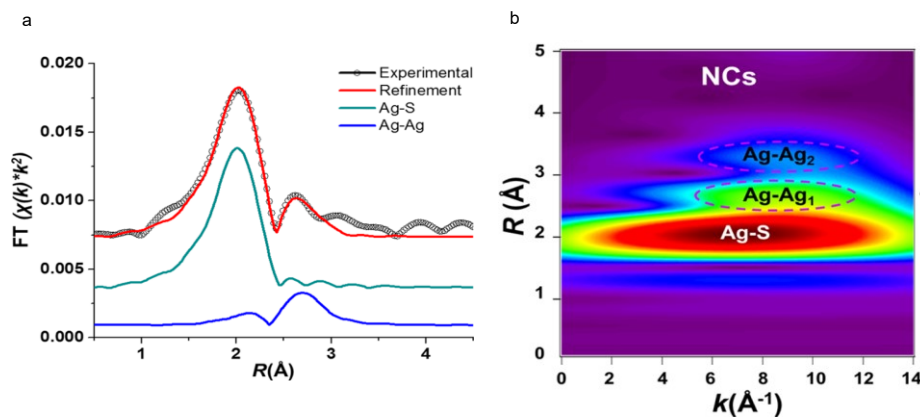


**Figure 2-5.** a) FT-EXAFS data for tiopronin-protected Ag NCs. b) Wavelet transformations of the EXAFS data for tiopronin-protected Ag NCs.<sup>39</sup> Copy right 2015, American Chemical Society.



### 2.2.3 Theoretical Simulation

The analysis of FT-EXAFS requires using a FEFF code to calculate the scattering amplitude and phase shift.<sup>81</sup> FEFF is based on Green's function. The calculations require the coordinates of each atom. The coordinates can come from known crystal structure or structure models from density functional theory (DFT) calculations. The electronic structure of absorbing atoms can be calculated by FEFF. A muffin-tin approximation is used, which means the potentials are estimated around the one atom with a specific radius, and the potentials between interstitial atoms are constant. Then, the calculation results can be applied to do the fitting of FT-EXAFS. At the same time, the simulated FT-EXAFS can be generated, which can be compared to the experimental data. In addition, the simulated XANES can also be obtained by FEFF. When FEFF does the calculations, one atom is defined as an absorbing atom. By changing the absorbing atom, the site-specific simulations can be carried out, which can help with the understanding of structure and properties of materials.

### 2.3 X-ray Photoelectron Spectroscopy (XPS)

Another useful X-ray technique is XPS, which can provide in-depth information about electronic properties of materials. It is often utilized as a complementary tool with XAS to study the electronic properties. XPS is based on the photoelectric effect.<sup>82</sup> In this technique, the X-ray source is generated from either a laboratory source or synchrotron radiation. The monochromatic X-rays are used to excite the electrons in the samples and then emitted electrons can be collected by the detector, as illustrated in **Figure 2-6**. The number of collected electrons versus binding energy can be plotted.

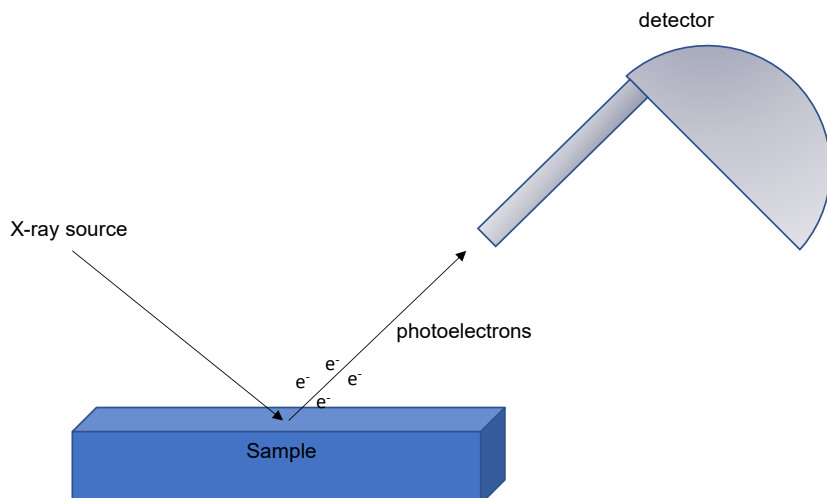


**Figure 2-6.** Scheme of generation and detection of photoelectrons of XPS instrument.

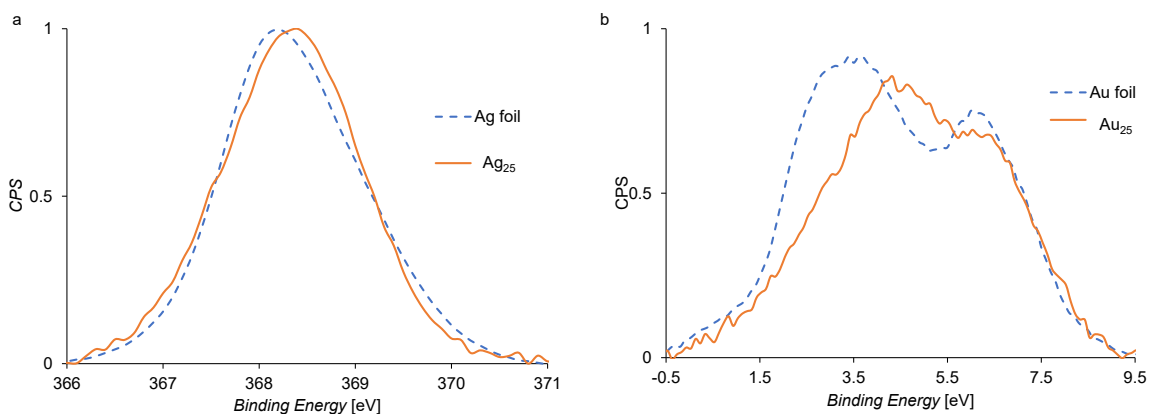


**Figure 2-7.** a) Core-level XPS spectra of Ag foil and Ag<sub>25</sub> NCs. b) Valence band XPS spectra of Au foil and Au<sub>25</sub> NCs.

XPS can be used to detect the electronic structure from inner core level to outer valence band. In general, the binding energy shift of core level can indicate the changes of coordination environment and chemical oxidation state of the element. Since the binding energy can be considered as the contribution from the initial state and final state of the system, the shifts are attributed to initial- or final-state effects. Initial-state effects are related to the intrinsic electronic structure of the materials, which can be altered by

charge transfer and interactions with ligands.<sup>83</sup> In addition, the change of electronic structure caused by passing from bulk to nanoscale is also considered as an initial-state effect.<sup>84</sup> Final-state effects are associated with the creation of core-hole and charge neutralization after excitation.<sup>83,84</sup> After excitation, an unscreened core-hole has been produced, and the system will rearrange remaining electrons. If the core-hole cannot be neutralized within a short time, the XPS binding energy will shift. Many studies have shown that the binding energy shift and the peak width of XPS spectra can be related to the size of nanomaterials.<sup>83,85-87</sup> As shown in **Figure 2-7a**, the core-level XPS spectrum of Ag<sub>25</sub> NCs show a positive binding energy shift. For transition metal NCs, the valence band XPS spectra can reflect the d-band of transition metals.<sup>88</sup> The peak width and d-band center position can be used to analyze their electronic properties. Typically, the valence band spectra can show a doublet peak due to spin-orbit splitting,<sup>85,89,90</sup> as shown in **Figure 2-7b**. Therefore, the electronic properties of NCs can be studied by XPS from core-level to valence band.

## Chapter 3 - Bonding Properties of $[\text{Ag}_{25}(\text{SR})_{18}]^-$ Nanocluster by X-ray Spectroscopy

*Manuscript to be submitted to Small* (Contributing authors: Chen, Z.; Walsh, A. G.; Zhu, M.; Zhang, P.) *The supporting information for this manuscript is including in Appendix A.*

### Contributions

M.Z. synthesized  $\text{Ag}_{25}(\text{SR})_{18}$  and  $\text{Au}_{25}(\text{SR})_{18}$  NCs. Z. C. carried out the Ag K-edge XAS measurements, performed the data analysis, and wrote the manuscript. P.Z. supervised Z.C. and helped revise the manuscript.

### 3.1 Introduction

Atomically precise noble metal nanoclusters (NCs) typically have a precise number of atoms, and their diameters are less than 2 nm, but they need to be protected by ligand groups such as phosphines and thiols.<sup>91</sup> Thiolate-protected noble metal NCs have attracted increasing attentions due to their unique properties. They have molecular-like behavior and show discrete electronic structures because of their small sizes, which give them special optical properties.<sup>92</sup> In addition, these materials have good stability because of their surface properties. Therefore, they can be applied in many different areas such as biology<sup>93-96</sup> and catalysis.<sup>97-99</sup> Although Ag and Au are in the same group in the periodic table, silver can be oxidized more easily than gold. Thus, the thiolate-protected Au NCs have been well studied in terms of their synthesis, structures and characterizations due to their high stability.<sup>100</sup> Recently, with the development of improved synthesis methods, more attention has been put on thiolate-protected Ag NCs and a few Ag NCs structures have been determined.<sup>99</sup>

Among the atomically precise Ag NCs reported, only 25-atom Ag NCs show matching analogues with Au NCs systems.<sup>101</sup>  $[\text{Ag}_{25}(\text{SR})_{18}]^-$  and  $[\text{Au}_{25}(\text{SR})_{18}]^-$  have similar crystal structures and a close number of free valence electrons. They are both negatively charged and both possess a  $1\text{S}^21\text{P}^6$  superatom electron configuration.<sup>49</sup> Moreover,  $\text{Ag}_{25}$  NCs show differences in structure from other atomically precise Ag NCs. For example,  $\text{Ag}_{25}$  has six 1D staple-like  $\text{Ag}_2\text{S}_3$  motifs, but other Ag NCs protected by pure thiolate ligands, like  $\text{Ag}_{44}$ , have 3D  $\text{Ag}_2\text{S}_5$  motifs.<sup>93</sup> Moreover, staple Ag atoms in  $\text{Ag}_{25}$  also show a different coordination environment than other silver thiolate compounds ( $\text{Ag}_3\text{S}_3$  units).<sup>102</sup> Hence,  $\text{Ag}_{25}$  shows differences from other Ag NCs but has similarities to Au NCs.

Since  $\text{Au}_{25}$  NCs are some of the most widely studied NCs, the close comparison between  $\text{Ag}_{25}$  and  $\text{Au}_{25}$  can provide an in-depth understanding of atomically precise 25-atom Ag NCs. Herein, we report the electronic properties of  $\text{Ag}_{25}$  using X-ray photoelectron spectroscopy (XPS) and compare them with electronic properties of  $\text{Au}_{25}$ . The bonding properties of  $\text{Ag}_{25}$  are studied using X-ray absorption spectroscopy (XAS). This technique can be used to analyze both structural and electronic properties with one full spectrum. Moreover, it has the flexibility to measure samples without the need for crystallization. XAS has been successfully applied to study ultra-small Ag and Au NCs for their structures and electronic properties.<sup>103–105</sup> However, the close comparison of XAS studies between  $\text{Ag}_{25}$  and  $\text{Au}_{25}$  is not feasible because different edges, corresponding to different electronic transition processes, were used.

## 3.2 Experimental Methods

### 3.2.1 Synthesis of Nanoclusters

The synthesis of Au<sub>25</sub> and Ag<sub>25</sub> were conducted by Prof. Zhu's group. Generally, the metal salt solutions were mixed with thiolate ligands to form metal thiolate intermediates, which were then reduced by NaBH<sub>4</sub> to obtain metal NCs. Details concerning the synthetic procedures can be found in the literature.<sup>64,106</sup>

### 3.2.2 XPS Measurements and Data Analysis

The XPS measurements of Ag<sub>25</sub> and the valence band measurement of Au<sub>25</sub> were performed with a Multilab 3000 XPS system manufactured by Thermo VG Scientific. The data was collected with an x-ray generated by Al irradiation having an energy of 1486.6 eV. The data calibration and component fitting were processed using CasaXPS software.<sup>107</sup> The binding energies were calibrated by using the carbon 1s peak for Ag and using the Fermi energy level for Au. The background was removed using the Shirley function. The component fitting of Ag 3d was performed by following the procedures used for the analysis of Au<sub>25</sub> in previous work.<sup>108</sup> The width of valence band was calculated using full width at half maximum (FWHM).

### 3.2.3 XAS Measurements and Data Analysis

The XAS measurements were conducted at the Sector 20-BM beamline of the Advance Photon Source (operating at 7.0 GeV) at Argonne National Laboratory in Argonne, IL, USA. The Au L<sub>3</sub>- edge data was collected in transmission mode, while the Ag K-edge data was collected in fluorescence mode. A Si (111) monochromator crystal with a harmonic rejection mirror was used to select the wavelength. The powders of Ag<sub>25</sub> and Au<sub>25</sub> were sealed in Kapton film pouches and were folded. The foil references were

simultaneously measured with each scan for the edge energy calibration at room temperature (RT). The low temperature (LT) measurement of Ag<sub>25</sub> was carried out at 90 K by using a liquid He cryostat.

The simulations of the Ag K-edge were done by using the FEFF8.2 computer code.<sup>81</sup> The simulation model only contained all of the Ag and S atoms without organic chains. For each site simulation, only one Ag atom was selected as the target atom. The simulation of Ag<sub>25</sub> was generated using a weighted average (the number of silver atoms in each site divided by the total number of silver atoms) y-axis of each site.

The EXAFS data fitting analysis of Ag<sub>25</sub> was performed using Artemis and Athena.<sup>109</sup> Both RT and LT data were analyzed using a k-weighting of 3. A k-range of 3.0-10.6 Å<sup>-1</sup> and fitting window of 0.8-3.5 Å were used for the RT data. For LT data, a longer k-range of 3.0-12.8 Å<sup>-1</sup> and a narrower fitting window of 1.7-3.0 Å were used. The quality of the RT data was worse than that of the LT data, so a shorter k-range could help reduce the amount of noise. In this case, a wider fitting window was used to reduce the number of variables in the fitting process. To further reduce the number of variables for multi-shell fitting, all CNs were fixed from the theoretical calculation of the crystal structure. The E<sub>0</sub> of three shells and the  $\sigma^2$  for two Ag-Ag shells were correlated. The amplitude reduction factors S<sub>0</sub><sup>2</sup> for both temperatures were determined from the foil that was measured simultaneously with the samples. They were fixed at 0.82 for both temperatures in the EXAFS fitting procedures. Wavelet transformations of the EXAFS data of Ag<sub>25</sub> and Au<sub>25</sub> at RT were performed by using the Morlet wave transform.<sup>78</sup>

### 3.3 Results and Discussion

#### 3.3.1 XPS Study of Electronic Properties

The core-level XPS spectra of Ag<sub>25</sub> and Ag foil are shown in **Figure 3-1a**. Ag<sub>25</sub> exhibits a shift of about 0.20 eV to higher binding energy compared with the Ag foil. Similarly, in the Au<sub>25</sub> system, a positive shift of 0.19 eV was also observed when compared with Au foil.<sup>108</sup> The capping of thiolate ligands and the small size of the NCs could cause the positive binding energy shifts.<sup>85,110</sup>

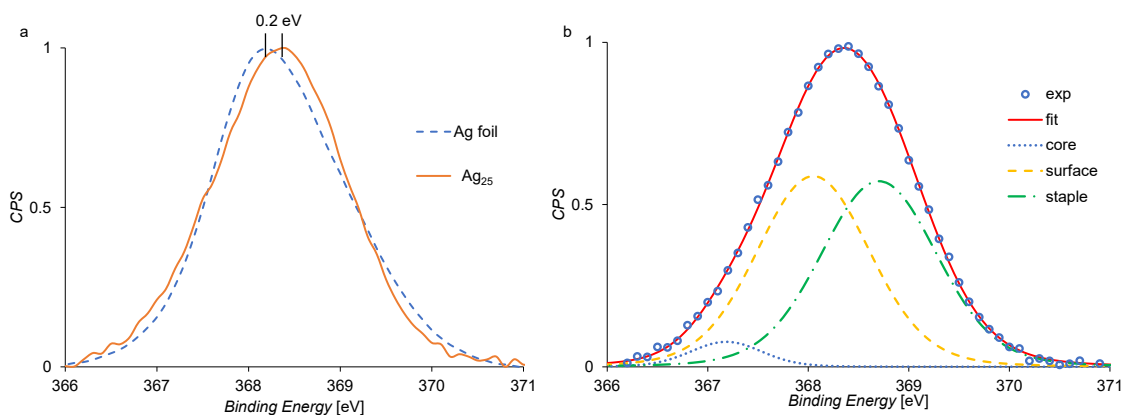


**Figure 3-1.** a) Ag 3d<sub>5/2</sub> XPS spectra of Ag<sub>25</sub> and Ag foil. b) Multiple-component fitting of Ag 3d<sub>5/2</sub> XPS spectrum of Ag<sub>25</sub>.

**Table 3-1.** Multiple-component fitting results of XPS core-level spectra of Ag<sub>25</sub> and Au<sub>25</sub>.

	Position (eV)		FWHM (eV)	
	Ag <sub>25</sub> (3d <sub>5/2</sub> )	Au <sub>25</sub> (4f <sub>5/2</sub> ) <sup>a)</sup>	Ag <sub>25</sub> (3d <sub>5/2</sub> )	Au <sub>25</sub> (4f <sub>5/2</sub> ) <sup>a)</sup>
Center	367.18	87.66	0.84	0.47
Surface	368.05	87.95	1.32	0.89
Staple	368.70	88.36	1.36	1.49
Surface- center	0.87	0.29	-	-
Staple- center	1.52	0.70	-	-

<sup>a)</sup> The results of Au<sub>25</sub> were borrowed from the literature.<sup>108</sup>



For a more detailed comparison between Ag<sub>25</sub> and Au<sub>25</sub>, multiple-component fitting of the core-level XPS spectra was carried out. The fitting results are displayed in **Figure 3-1b** and **Table 3-1**. The peak was fitted using three components. Based on the reported crystal structures of these two NCs, Ag<sub>25</sub> and Au<sub>25</sub> have similar structures. Their crystal structures are shown in Appendix Figure A1. They have one center atom surrounded by 12 atoms to form an icosahedral metal core. Then, the remaining 12 atoms can form six M<sub>2</sub>S<sub>3</sub> (M=Ag, Au) “staple” motifs to protect the M<sub>13</sub> metal core.<sup>111,112</sup> Thus, the peak area ratio of the three components was constrained to 1:12:12 for Ag<sub>center</sub>:Ag<sub>surface</sub>:Ag<sub>staple</sub>. For both nanoclusters, the binding energies increase upon moving from the center, to the surface, and then to the staple. This result suggests that the atoms at staple sites are less metallic due to their interaction with thiolate ligands. The surface atoms have a mixture of metallic and non-metallic nature. Generally, the electronic properties of species are analyzed by the XPS binding energy shift. However, the binding energy shift can be caused by the initial state effect and the final state effect in XPS spectra.<sup>87</sup> For ultrasmall thiolate-protected clusters, it is possible that the positive binding energy shift is due to the final state effect, because the core hole cannot be neutralized within a short time after excitation.<sup>86</sup> Then, the positive shift in the binding energy of the clusters can be observed in the XPS spectra when the bulk compounds are used as reference. In this study, the same amount of shift was observed for both clusters when compared with bulk references. Thus, bulk materials are not good references for the study of ultrasmall clusters.

To closely compare the differences between Ag<sub>25</sub> and Au<sub>25</sub>, the energy shifts of the surface and staple sites relative to the center atom were calculated. Since the central

atom is the most metallic site in each cluster, it can be used as a good reference for the study of their electronic properties. The final state effect can be excluded in this case. Interestingly, Ag<sub>25</sub> shows larger energy differences than Au<sub>25</sub>. Ag atoms at the surface and staple positions have more positive charge than Au atoms at same sites compared to the center atom, which could be caused by the differences between Ag and Au in electronegativity (Ag:1.39; Au: 2.54). Ag has lower electronegativity than Au and S. Thus, Ag-S bonds would be more polar than Au-S bonds. Ag atoms can lose more electrons than Au atoms and they can possess more positive charge. The results from multiple-component fitting are in good agreement with the Bader charge analysis of these two NCs.<sup>113,114</sup> The M<sub>13</sub> metal core (Bader charge of Ag<sub>13</sub>: 0.092 e<sup>-</sup>; Au<sub>13</sub>: 0.027e<sup>-</sup>) has a lower charge than the total charge of atoms at staple sites for both clusters (Ag staple: 0.214 e<sup>-</sup>; Au staple:0.086 e<sup>-</sup>). The Bader charge analysis of Ag<sub>25</sub> and Au<sub>25</sub> show that all Ag atoms possess higher charge than Au atoms, and the thiolate ligands in Ag NCs have more electrons than those in Au NCs. Thus, more electrons are withdrawn by ligands in the Ag NC system because of the lower electronegativity of Ag. The difference in charge between Ag and Au is more pronounced for the staple sites in the Bader charge analysis, which is similar to the observation from the core-level XPS study. This result indicates that thiolate ligands withdraw electrons more effectively from the staple sites than surface sites. Since Ag-S bonds are more polar than Au-S bonds, the impact of thiolate ligands on the electronic properties of surface and staple sites is different in Ag than in Au NCs.

The valence bands of the two nanoclusters were also investigated. The spectra are presented in **Figure 3-2**, and the band position and width are listed in **Table 3-2**. Ag<sub>25</sub> and Au<sub>25</sub> clusters show 0.30 eV and 0.38 eV of positive band center shift, respectively,

which is consistent with the observation from core-level XPS data. The doublet peak in gold is due to spin-orbit splitting. The splitting of gold is more apparent than silver. Therefore, the valence band of Ag is not well resolved, and appears as a broad peak. Notably, the two nanoclusters have narrower peaks than the bulk materials. The band widths of the two NCs are about 80% of the band width for the bulk materials. The clusters show about 0.45 eV and 0.90 eV narrower band width for Ag<sub>25</sub> and Au<sub>25</sub>, respectively. The narrowing of the peaks could be caused by the nanosize of the clusters. The small size of the NCs means that the atoms have less coordinated nearest neighbors, which could induce the decrease in the band width.<sup>90</sup> Additionally, the Au NCs system shows a larger narrowing effect because the band width for Au NCs is larger than that for Ag NCs. This narrowing is likely due to the relativistic effect of gold, which can lead to strong s-d hybridization and d-d interaction in gold.<sup>115</sup> The relativistic effect can lower the energy of the 6s orbital and raise the energy of the 5d orbitals. The small energy between the s and d orbitals in gold causes a stronger s-d hybridization, which can further induce the increase in overlap between the 5d orbitals of gold atoms.

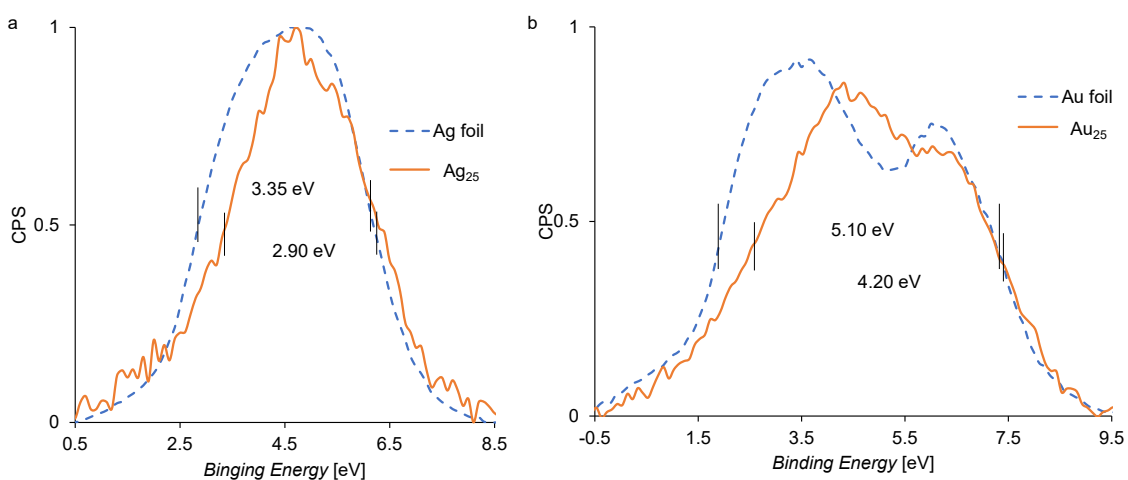


**Figure 3-2.** a) Ag 4d XPS spectra of Ag<sub>25</sub> and Ag foil. b) Au 5d XPS spectra of Au<sub>25</sub> and Au foil.

**Table 3-2.** Valence band center position and width of 25-atom NCs and foils.

	<b>Ag<sub>25</sub></b>	<b>Ag foil</b>	<b>Au<sub>25</sub></b>	<b>Au foil</b>
Band center (eV)	4.85	4.55	4.93	4.55
FWHM (eV)	2.90	3.35	4.20	5.10

### 3.3.2 XAS Study of Ag<sub>25</sub>

X-ray absorption near-edge structure (XANES) spectra were also used to probe the electronic properties, because XANES can correspond to electronic transitions from the core level to unoccupied states. Ag<sub>25</sub> and Au<sub>25</sub> were measured at different edges, which correspond to different electron transitions. Thus, the close comparison between their XANES spectra is not feasible; only the Ag<sub>25</sub> XANES results will be discussed. The XANES and first derivatives spectra are shown in **Figure 3-3a,b**. Interestingly, the first derivative spectrum of Ag<sub>25</sub> shows a large differences in peak features from Ag foil. In **Figure 3-3b**, Ag foil shows a small shoulder peak for the first peak of the first derivative spectrum, which is absent in Ag<sub>25</sub> clusters. The peak width of the first peak is narrower for Ag<sub>25</sub> clusters than for Ag foil. The feature at around 25535 eV (indicated by an arrow) shows a broad peak for the Ag<sub>25</sub> cluster, but Ag foil has a valley at this position.

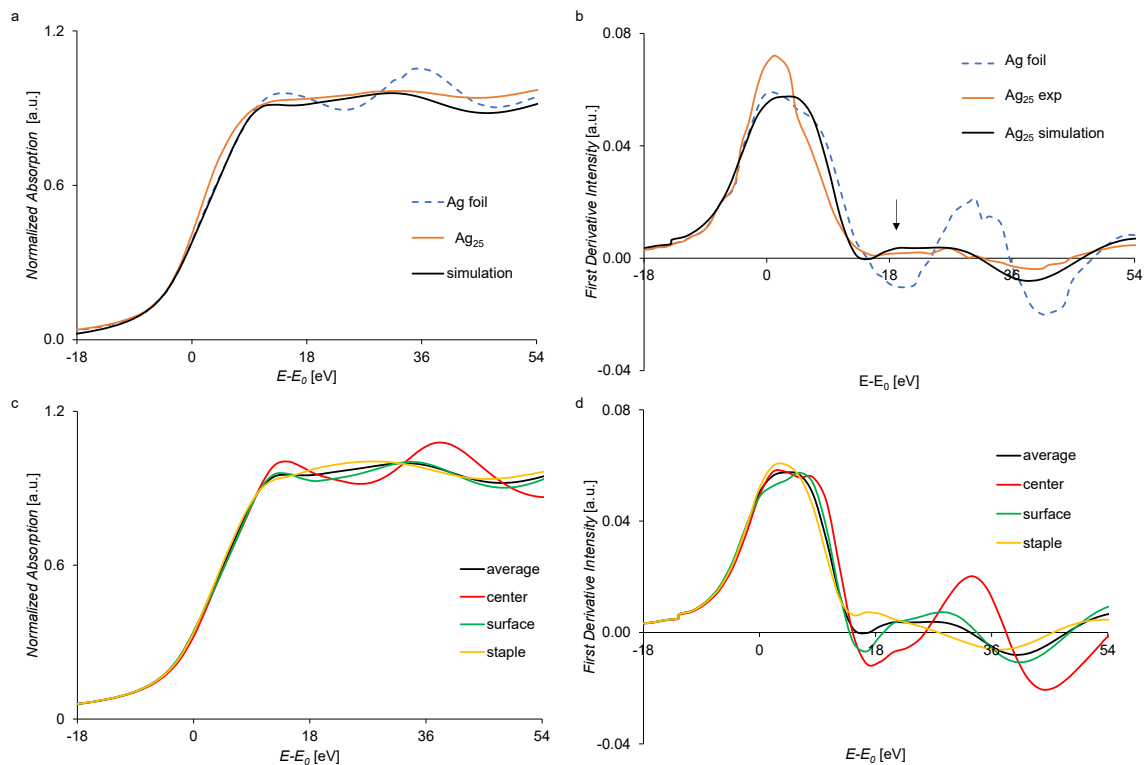


**Figure 3-3.** a) Ag K-edge XANES spectra and b) first derivatives of the XANES spectra for Ag foil, experimental data, and averaged simulation of Ag<sub>25</sub>. c) Simulations of XANES spectra and d) first derivatives of the simulated XANES spectra for each site of Ag<sub>25</sub>.

To understand the differences in peak shapes and peak widths between the Ag<sub>25</sub> cluster and Ag foil, the simulations of the average Ag K-edge XANES spectrum and that for each site of the Ag<sub>25</sub> cluster were performed. In **Figure 3-3a,b**, the simulation of the Ag<sub>25</sub> XANES spectrum and its first derivative have similar features as the experimental data, which means that the simulation method is reliable. The site-specific simulations are shown in **Figure 3-3c, d**. The center site is the most metallic site, and its first peak in the first derivative spectrum exhibits a doublet, which agrees with the observation from Ag foil. The average spectrum is the simulation of the Ag<sub>25</sub> cluster, which uses a weighted average of each site. The shape of the first peak in the averaged Ag<sub>25</sub> first derivative simulation is similar with the shape of the staple site simulation. They both show single

peaks, and the peak width is narrower than that of the metallic center site. In addition, the center site shows a deep valley after the first peak, whereas the staple site exhibits a broad peak feature. Therefore, the observation of a single, narrow peak in the experimental first derivative spectrum of Ag<sub>25</sub>, and the broad peak feature after the first peak can be explained by the presence of thiolate ligands in the nanocluster system. Moreover, the overall shape of the Ag<sub>25</sub> XANES spectrum exhibits different features from the Ag foil XANES spectrum, but contains the shape of the XANES spectra for Ag<sub>2</sub>S and Ag-thiol.<sup>116</sup> These similarities further prove that the Ag<sub>2</sub>S<sub>3</sub> staple motifs have a large impact on the electronic properties of the clusters. The site-specific analysis of the XANES spectra is a quick method to study surface modified Ag NCs because they can work as fingerprints.

To investigate the bonding properties of the Ag NCs, the EXAFS study of Ag<sub>25</sub> at different temperatures was performed. Since the crystal structure of the Ag<sub>25</sub> NCs has been reported, the fitting model for EXAFS could be built. Based on the bond distribution, there exists one metal-S shell and two metal-metal shells (**Figure 3-4**). The shorter Ag-Ag bonds are bonds between the center Ag atom and Ag atoms at icosahedral sites. The longer Ag-Ag bonds correspond to bonds between Ag atoms at surface sites, and bonds between icosahedral core and staples. The crystal structure and bond distribution of Ag<sub>25</sub> are slightly different from Au<sub>25</sub>. The only noticeable structural difference between these two clusters is that there are three distorted staple Ag atoms in Ag<sub>25</sub>,<sup>64</sup> which are shown in blue in Appendix Figure A1. In Au<sub>25</sub> clusters, the Au<sub>13</sub> metal core includes not only the bonds from the center core to surface Au atoms, but also several short bonds between surface Au atoms.<sup>64</sup> The detailed comparison of the bond

distribution is shown in Appendix Figure A2. Therefore, there are more metallic bonds in the Au<sub>13</sub> metal core than that in the Ag<sub>13</sub> metal core.

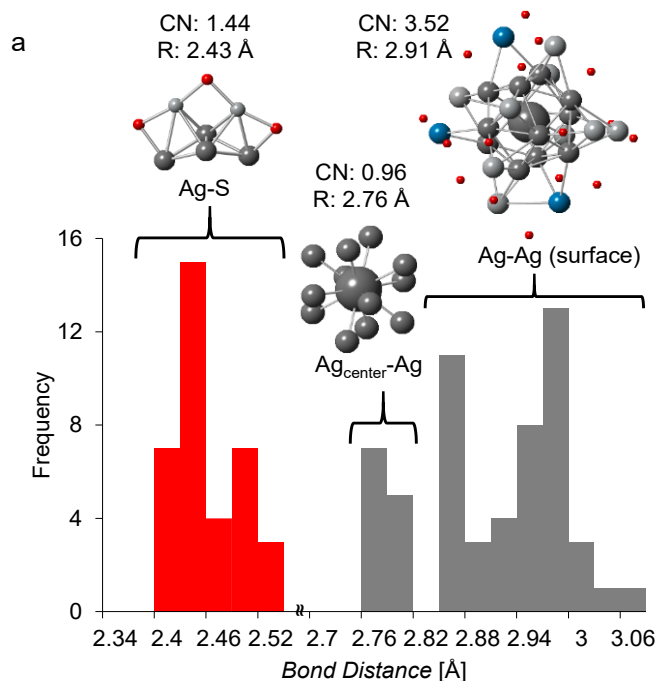


**Figure 3-4.** Bond distribution of Ag<sub>25</sub>(SR)<sub>18</sub> and theoretical CNs and bond distances for each shell. Red: S; Light grey: staple Ag; Dark grey: metal core Ag; Blue: distorted staple Ag.

The theoretical CNs could be calculated based on the model, which are used as fixed values in the FT-EXAFS fitting of Ag<sub>25</sub> to reduce the number of variables. In the EXAFS fitting analysis, Ag-Ag bonds longer than 3.06 Å were not included, which are considered as long-distance interactions. In the Ag K-edge FT-EXAFS spectrum(**Figure 3-5**), there are two major peaks. The peak centered at around 2 Å corresponds to Ag-S bonds. The other peak between 2-3 Å is contributed by Ag-Ag bonds. The intensity of metal-metal bond peak is much lower for Ag NCs than Ag foil, indicating the small size of the NCs. Another way to visualize the EXAFS data is using wavelet transformations (WT) plots. The WT-EXAFS spectrum of Ag<sub>25</sub> at RT is shown in **Figure 3-5b**. The maximum at R~2 Å and k~6 Å<sup>-1</sup> corresponds to the metal-S shell, and the island centered

at  $R \sim 2.7 \text{ \AA}$  and  $k \sim 6 \text{ \AA}^{-1}$  is contributed by metal-metal shells. The temperature effect on the cluster was also investigated. The EXAFS spectra at RT and LT were collected. The fitting results are shown in **Figure 3-5c,d** and the fitting structural parameters are summarized in **Table 3-3**. The bond distances in  $\text{Ag}_{25}$  are close to the theoretical bond distances obtained from its crystal structure, suggesting the validation of the EXAFS fittings. Comparing the EXAFS results at both RT and LT, the bond distances are unchanged within uncertainty, which is different from the temperature effect on  $\text{Au}_{25}$ . In  $\text{Au}_{25}$ , the metal core shows contraction as the temperature is decreased.<sup>103</sup> Thus,  $\text{Ag}_{25}$  exhibits less sensitivity to the temperature changes, and the core of  $\text{Ag}_{25}$  shows more molecular-like behavior than  $\text{Au}_{25}$ . This result could be due to the  $\text{Ag}_{13}$  core being less metallic than  $\text{Au}_{13}$ . In addition, Ag-Ag bond distances in the  $\text{Ag}_{13}$  core (around  $2.74 \text{ \AA}$ ) are shorter than Au-Au bond distances (roughly  $2.82 \text{ \AA}$ ) in  $\text{Au}_{13}$ . The  $\text{Ag}_{25}$  cluster has a smaller metal core than  $\text{Au}_{25}$ , because  $\text{Ag}_{13}$  only has center-surface interactions, whereas  $\text{Au}_{13}$  has center-surface and surface-surface interactions. Moreover, the possible reason for the unchanged of Ag-Ag surface bond distances could be that the surface Ag atoms are directly linked to thiolate ligands, and their positions can be regulated by the ligands due to the  $\pi$ - $\pi$  interactions of the aromatic rings. It is hard to change the bond distances of surface Ag-Ag bonds.



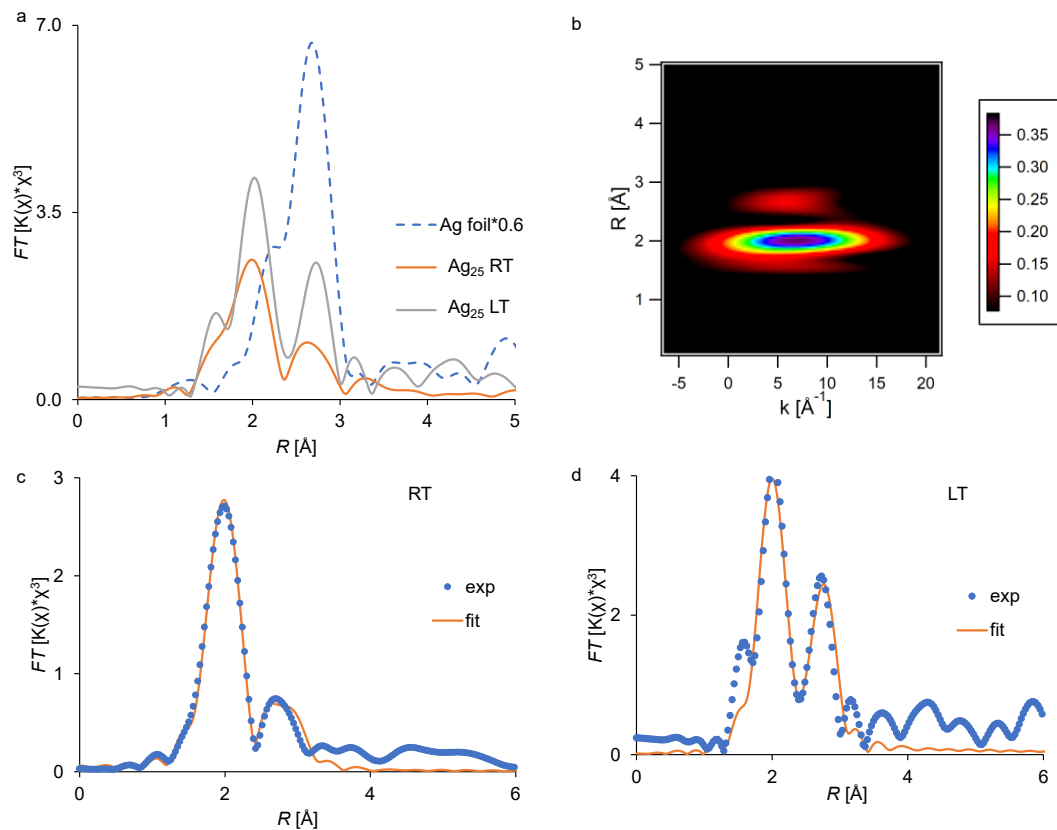


**Figure 3-5.** a) FT-EXAFS spectra of  $\text{Ag}_{25}$  at two different temperatures and Ag foil. b) Wavelet transformations of the EXAFS data for  $\text{Ag}_{25}$  at room temperature c) Fitting of the FT-EXAFS spectrum of  $\text{Ag}_{25}$  at room temperature. d) Fitting of the FT-EXAFS spectrum of  $\text{Ag}_{25}$  at low temperature (90 K).

**Table 3-3.** Structural parameters of  $\text{Ag}_{25}$  at RT and LT.

	Shell	CN	R (Å)	$\sigma^2$ (Å <sup>2</sup> )	$\Delta E_0$ (eV)	R-factor
$\text{Ag}_{25}$ RT	Ag-S	1.44	2.467 (8)	0.0043 (5)	2 (1)	0.0088
	Center-Ag	0.96	2.74 (7)	0.021 (4)		
	Ag-Ag	3.52	2.92 (2)			
$\text{Ag}_{25}$ LT	Ag-S	1.44	2.48 (1)	0.0030 (9)	4 (3)	0.0172
	Center-Ag	0.96	2.75 (8)	0.011 (2)		
	Ag-Ag	3.52	2.90 (3)			

### 3.4 Summary

In summary, we have studied the electronic and bonding properties of  $\text{Ag}_{25}$  by using X-ray spectroscopy techniques. By using the central atoms as a reference, a unique XPS analysis method was developed to study the electronic property of this ultrasmall cluster. This method can exclude the final state effect on the XPS binding energy shift. By comparing the XPS results of  $\text{Ag}_{25}$  and  $\text{Au}_{25}$ , Ag atoms in the staple and surface of  $\text{Ag}_{25}$  show different charge transfer behavior from Au atoms in same sites of  $\text{Au}_{25}$ . The relative charge of the Ag atoms in the staple and surface sites was found to be higher than that of Au atoms in the same positions in that more electrons were withdrawn by thiolate ligands in  $\text{Ag}_{25}$  than in  $\text{Au}_{25}$ . The valence band of both nanoclusters exhibited a positive shift of the center position and narrower peaks compared to bulk materials. From the site-specific simulations of the XANES spectra, the important features of the  $\text{Ag}_{25}$  XANES spectra were attributed to the staple sites, suggesting the  $\text{Ag}_2\text{S}_3$  staple motifs had a large impact on the electronic properties of the  $\text{Ag}_{25}$  cluster. Furthermore,  $\text{Ag}_{25}$  demonstrated unique temperature-dependent bonding properties. The observation of unchanged bond distances as the temperature changed indicated the molecular-like behavior of  $\text{Ag}_{25}$ , while the  $\text{Ag}_{13}$  core had less metallic bonds than the  $\text{Au}_{13}$  core. Overall, the properties of thiolate-protected Ag NCs were probed from site-specific perspective, which offers an in-depth understanding of the relationship between structure and properties. The unique XPS analysis method can be applied to study electronic properties of other Ag NCs.

## Chapter 4 - The Structure and Property of Ag Nanoclusters Confined in Zeolites

### 4.1 Introduction

Bare Ag NCs are not stable because of their high surface energy, but they have high catalytic activity due to existence of uncoordinated active sites.<sup>69,117</sup> To solve the problem of cluster aggregation, different materials have been used to stabilize and protect small NCs.<sup>118-123</sup> In previous chapter, Ag NCs protected by thiolate ligands were discussed. Another way to protect Ag NCs is using hard templates such as zeolites. Zeolites are porous materials with high thermal stability, which are good materials for catalytic reactions.<sup>124</sup> In addition, the porous material zeolite can not only stabilize the Ag NCs, but also can have synergistic effect with metal species in catalytic reaction.<sup>125</sup> Their porous cage structure also can help improve the selectivity of a reaction.<sup>126</sup> There are many different approaches to synthesize Ag NCs confined in zeolites.<sup>65,69,127,128</sup> The metal precursor can be introduced into zeolite by in situ encapsulation method or post-synthesis encapsulation method. One typical example of the latter one is the ion-exchange method. Generally, zeolite frameworks have negative charge, which are balanced by cations.<sup>129</sup> Since they have high ion-exchange ability, those cations can be replaced by Ag ions.<sup>130</sup> Then, the formation of metallic Ag NCs can be done by reduction of Ag ions. The control of particle size is achievable by modifying the synthetic conditions. Then, the properties of metal NCs can be altered by tuning the particle size.<sup>131,132</sup> One way to control the size of particles is to regulate the concentration of metal ions. The number of cations that can be exchanged by metal ions is important to determine the cluster sizes.<sup>133</sup> If a different amounts of metal ions are used, the cluster size can be changed. The porous structure of zeolites can also help in controlling the size of particles.<sup>66,134,135</sup> The size,

shape and dimensions of pores are controllable during the synthesis of zeolites. Then, the particle size can be changed by regulating the available pore space.

In this work, zeolite Y and mordenite (MOR) were used to investigate the control of particle size by using different types of zeolites. The Ag NCs synthesized by using different concentrations of Ag ions were also studied. The size and structural information of samples were characterized by TEM and XAS. Their electronic properties were also investigated by XAS. Finally, the catalytic activity of Ag@Zeolite Y with 1.0 weight percentage (wt%) loading was tested for the styrene oxidation reaction.

## 4.2 Experiment Methods

### 4.2.1 Synthesis of Nanoclusters

The synthesis of Ag NCs in zeolites was conducted by ion-exchange method followed by reduction, as shown in **Figure 4-1**. The AgNO<sub>3</sub> precursor was used to prepare 2.4 x 10<sup>-3</sup> M metal stock solution. Based on the metal loading weight percentage, different amounts of AgNO<sub>3</sub> stock solution were added into 100 mg zeolite powder. The mixtures were stirred for 24 hours under dark conditions. After ion-exchange, the solids were separated from the liquid by centrifugation. The solids were washed by deionized water and ethanol at least three times to make sure the extra Ag ions were washed away. Then, the solids were redispersed into deionized water. The freshly prepared NaBH<sub>4</sub> solutions were added to reduce Ag ions to form Ag NCs. The excess amount of NaBH<sub>4</sub> solutions (molar ratio Ag: NaBH<sub>4</sub> = 1: 10) was used to make sure all Ag ions can be reduced. After 1 hour, the solutions became yellow-brown, as shown in **Figure 4-2**, indicating the successful reduction of Ag ions to Ag NCs.<sup>136</sup> The solutions of samples

with higher concentration have darker color. Finally, the solids were separated and washed by deionized water and ethanol, and dried for 24 hours.

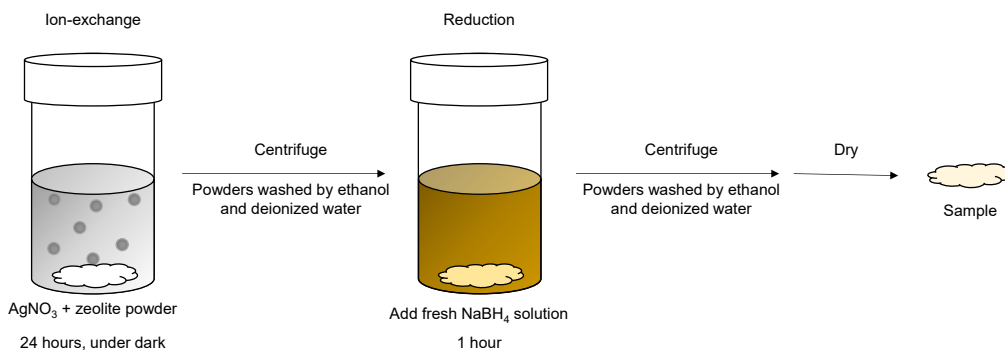


**Figure 4-1.** Schematic illustration of synthesis method for Ag NCs confined within zeolites

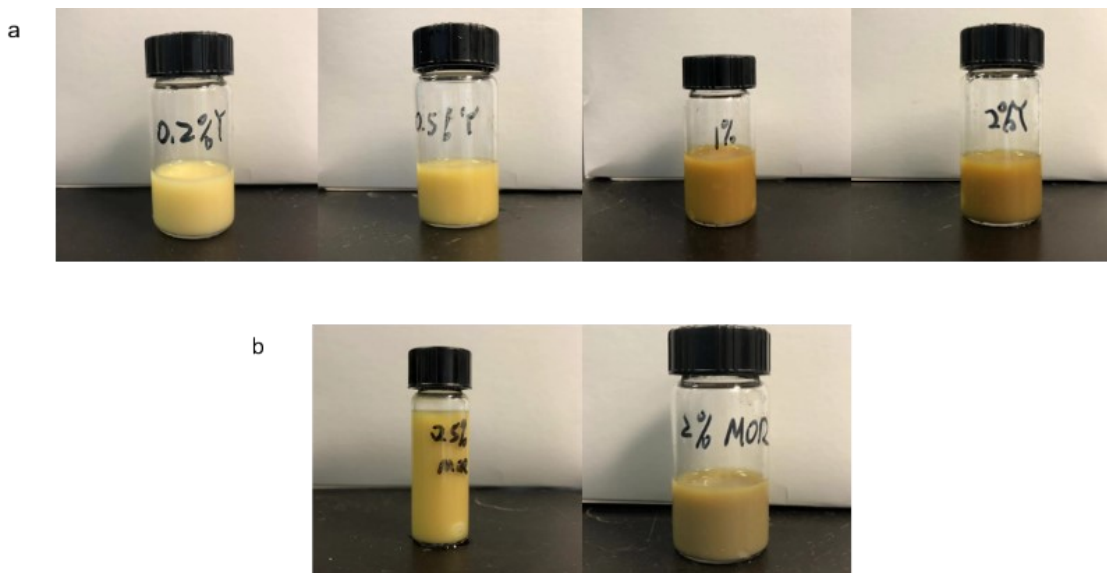


**Figure 4-2.** Pictures of a) Ag@Zeolite Y solutions and b) Ag@MOR solutions after reduction. The concentration increases from the left to the right.

#### 4.2.2 TEM Measurements

The transmission electronic microscopy (TEM) of these samples was measured at Xiamen University, China. The TECNAI F-30 high-resolution TEM operated at 300 kV was used. This microscopy is equipped with field-emission electron gun, which can

provide high resolution measurements. Condenser lens were used to focus the electron beam from electron gun. The focused beam was shone through the prepared samples. Then, the transmitted beam was focused by the objective lens into an image on charge coupled device. The image was passed down onto the screen by intermediate and projector lenses. The powder samples were dispersed in ethanol and then the mixture was ultrasonicated. A drop of suspension was casted onto a copper grid. The grid was dried to make sure all solvents were evaporated before measurements. Different areas of each sample were selected, and the magnifications were adjusted from low to high.

#### 4.2.3 XAS Measurements and Data Analysis

XAS measurement of all samples were conducted at Beamline Sector 20 of the APS (operating at 7.0 GeV) at Argonne National Laboratory. The Ag K-edge spectra were collected in fluorescence mode. The powders of samples were spread in Kapton tapes, and then the tapes were folded. The Ag foil reference was measured simultaneously in transmission mode. The fittings of FT-EXAFS data were performed by Athena and Artemis.<sup>109</sup> k-weight of 3 was used for all data fittings. The amplitude reduction factor, 0.79, was obtained from fitting of the Ag foil, and it was fixed for all fittings. For two-shell fittings,  $E_0$  was correlated for both shells. The k range of 3-12  $\text{\AA}^{-1}$  was used for Fourier transformation. The R range of 1.8 -3.1 $\text{\AA}$  was applied for one-shell fittings. The wider R range of 1.2-3.0  $\text{\AA}$  and 1.5-3.1  $\text{\AA}$  were used for two-shell fittings of 0.5 wt% Ag@MOR and 1.0 wt% Ag@Zeolite Y, respectively.

#### 4.2.4 Catalytic Reaction

The styrene oxidation reaction was used to test the catalytic activities, as shown in **Figure 4-3**. The catalytic reaction of 1.0 wt% Ag@Zeolite Y was performed in a round-

bottom flask. A 10 mg sample was added into 5 mL acetonitrile. The molar ratio 1:1000 was used for Ag: styrene. The appropriate amount of styrene was added. The flask was put into 80 °C oil bath and stirred for 5 minutes. After that, 5 mL tert-butyl hydroperoxide (TBHP) was added into solution to start the reaction under reflux condition. 0.1 mL of reaction solution was taken every two hours. The reaction proceeded for 12 hours. 500 MHz <sup>1</sup>H nuclear magnetic resonance (NMR) was used to analyze the reaction solutions at different time to monitor the reaction.

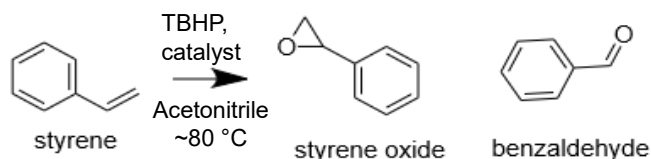


**Figure 4-3.** Styrene oxidation reaction with experimental reaction conditions.

## 4.3 Results and Discussion

### 4.3.1 Silver Nanoclusters in Zeolite Y

Four samples with different concentrations of Ag@zeolite Y were studied. The TEM of four samples are shown in **Figure 4-4**. For low concentration sample of 0.2 wt% Ag@Zeolite Y, it is difficult to visualize the small individual particles from images. From image of 0.5 wt% Ag@Zeolite Y, a few large particles are outside the zeolite framework. However, it looks similar to the image of 0.2 wt% Ag sample from a high-resolution image, indicating majority of particles are small and are confined within zeolites. When concentration of Ag precursor increases to 1.0 wt%, particles can be clearly observed. At 2.0 wt%, more particles are formed, and some of them are on the surface of zeolite. The size of particles also becomes larger, but their diameters are still less than 10 nm.

Therefore, it can be concluded that small Ag NCs were successfully formed within zeolites at different concentrations of Ag ions.

The XAS was used to characterize these samples. XANES can be used as a fingerprint to qualitatively study the samples. The Ag K-edge XANES spectra and their first derivative spectra are shown in **Figure 4-5**. The XANES spectra of samples show similar oscillation patterns to the spectrum of Ag foil, indicating most Ag atoms in samples are metallic Ag having similar coordination environment as the Ag atoms in the Ag foil. The intensity of the first peak following absorption edge decreases as the concentration changes from low to high, indicating they are slightly different in oxidation state. Interestingly, the XANES spectrum of 0.5 wt% Ag@Zeolite Y overlaps with the spectrum of 0.2 wt% Ag sample. Therefore, particles in 0.5 wt% Ag sample should have similar structure and size as particles in 0.2 wt% sample. This result further proves that a large percentage of Ag particles in 0.5 wt% sample should be as small as particles in the 0.2 wt% sample, although large particles are observed in TEM images. The small change of concentration shows no obvious change in structure and particle size. From their first derivative spectra of XANES (**Figure 4-5b**), the spectra of four samples exhibit narrower and more intense first peaks than bulk Ag. The change of peak width and intensity could be related to the size of NCs. The spectra of samples with small size tend to have narrower and more intense peaks.



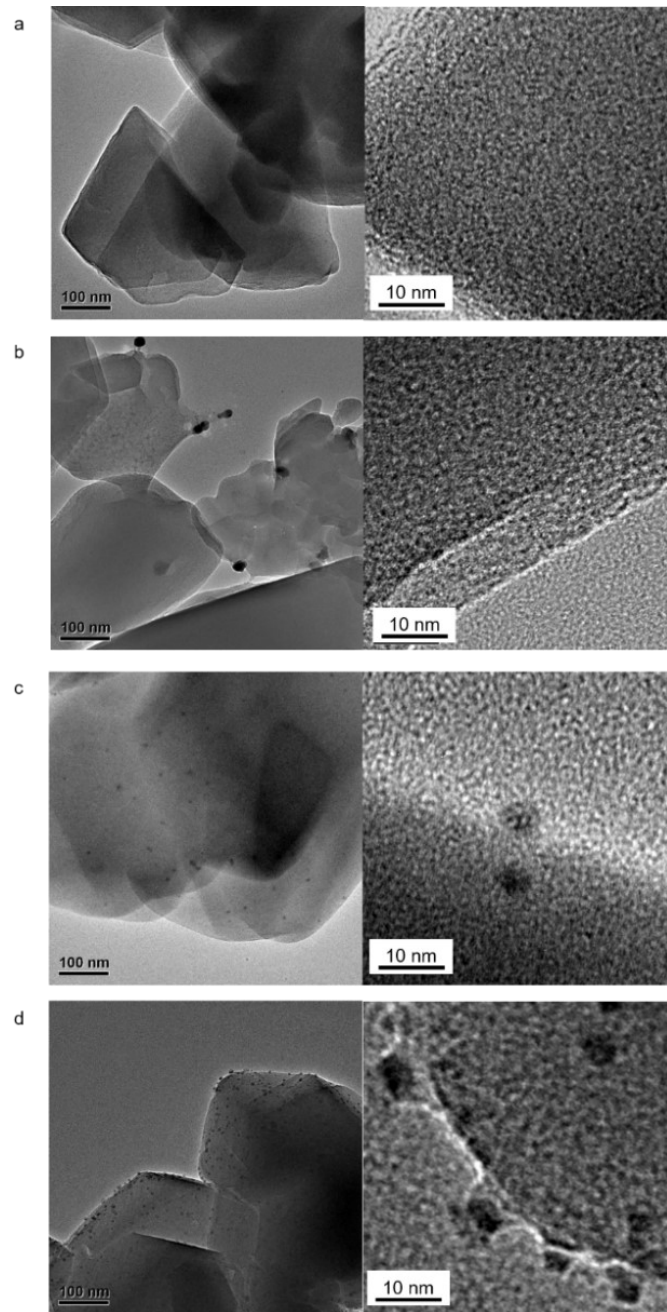


**Figure 4-4.** TEM images of a) 0.2 wt% b) 0.5 wt% c) 1.0 wt% d)2.0 wt% Ag@Zeolite Y.

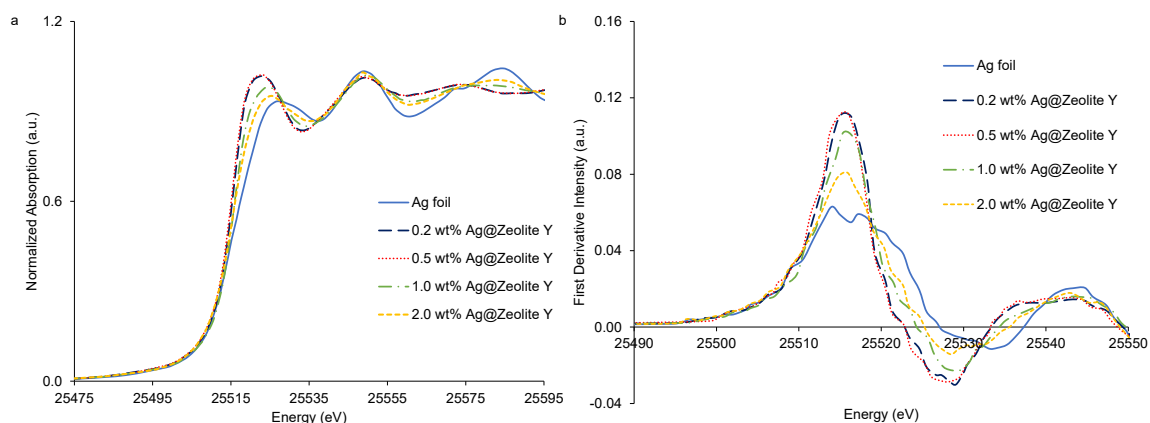


**Figure 4-5.** a) Ag K-edge XANES spectra of Ag@Zeolite Y samples and foil. b) first derivative spectra of XANES for Ag@Zeolite Y samples and foil.

The more detailed structural information is obtained from EXAFS. The Ag K-edge FT-EXAFS spectra are displayed in **Figure 4-6**. The spectra of all samples show a major peak between 2 and 3 Å, which corresponds to a Ag-Ag shell. The peak intensity of the Ag-Ag shell is lower than that in the spectrum of Ag foil, indicating small size of samples. Although particles were not observed from TEM images for the low concentration samples, the existence of the Ag-Ag shell indicates the formation of Ag NCs. For the 0.5 wt% sample, some large particles are formed outside the framework, but FT-EXAFS results show a low intensity peak for the Ag-Ag shell, which is similar to 0.2 wt% sample. This observation is consistent with XANES results. Thus, the percentage of large particles is small in the 0.5 wt% sample, and most particles should be inside the zeolites. In the FT-EXAFS spectra, the peak height can be related to the CNs. The sample with large CNs tends to have a higher peak. Interestingly, the peak intensity of the Ag-Ag shell becomes higher with the increase of concentration in this study. This result is similar to a previous reported study of Ag NPs within zeolites.<sup>137</sup> As the concentration of silver compound increases, more silver ions can be exchanged into the zeolite, and then they can be reduced to form larger clusters. In addition, when the concentration is high, it

is possible the amount of exchanged silver ions exceeded the capacity. Some of them could immigrate to the surface of zeolite and form large particles, as shown in TEM image **Figure 4-4d**.

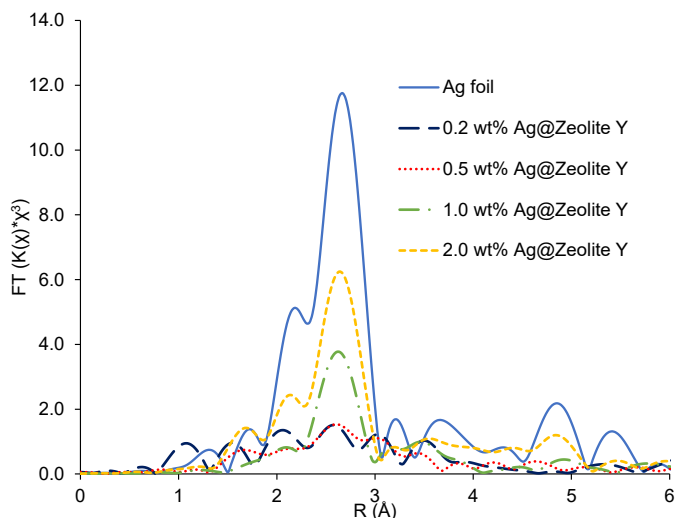


**Figure 4-6.** Ag K-edge FT-EXAFS spectra of four samples and Ag foil.

The fittings of FT-EXAFS spectra were performed to obtain structural parameters of the samples. The concentrations of 0.2 wt% and 0.5 wt% samples are too low to have good quality data for FT-EXAFS fittings. Only 1.0 wt% and 2.0 wt% were analyzed quantitatively. The fittings of FT-EXAFS spectra and results are shown in **Figure 4-7** and **Table 4-1**. Firstly, Ag-Ag one-shell fittings were applied to both samples. 1.0 wt% sample shows a smaller CN for Ag-Ag shell than 2.0 wt% sample, indicating smaller size of Ag NCs in 1.0 wt% sample. In FT-EXAFS spectra, there is a small peak at about 2.1 Å. It is possible that this peak is due to the Ag-O shell. Thus, two-shell fittings were used for both samples. However, only 1.0 wt% sample shows the improvement of fitting compared to one-shell fitting results. The smaller R-factor of two-shell fitting than that of one-shell fitting indicates the better fitting quality of new fitting method. The two-shell fitting results show similar CN, bond distance of Ag-Ag shell to the one-shell fitting

results, further indicating the validation of two-shell fitting. Notably, the Ag-O bond distances in 1.0 wt% sample are 2.46 Å, which are longer than the typical Ag-O bond distances in oxidized Ag NCs.<sup>138</sup> The long Ag-O bond distances suggest that there are interactions between Ag NCs and the oxygen in zeolite frameworks. The non-covalent interactions could be London dispersion forces.<sup>66</sup> This result can be related to the observation in TEM images. The TEM images show that most particles are inside the framework for 1.0 wt% sample. The possibility of oxidization of Ag NCs with protection is low. It is likely the protected Ag NCs inside zeolite can have interactions with the framework.

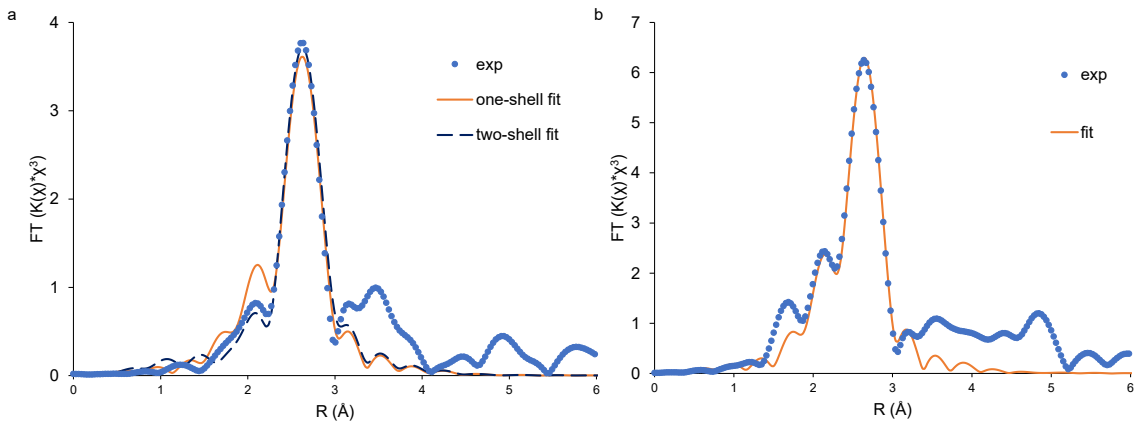


**Figure 4-7.** Fittings of FT-EXAFS spectra of a) 1.0 wt% Ag@Zeolite Y and b) 2.0 wt% Ag@Zeolite Y.

**Table 4-1.** Structural parameters of 1.0 wt% Ag@Zeolite Y and 2.0 wt% Ag@Zeolite Y as obtained from FT-EXAFS fittings.

	Shell	CN	R (Å)	$\sigma^2$ (Å <sup>2</sup> )	$\Delta E_0$ (eV)	R-factor	
1.0%	One-shell	Ag-Ag	5 (2)	2.86 (2)	0.012 (3)	-4 (2)	0.031
	Two-shell	Ag-O	2 (1)	2.46 (3)	0.013 (2)	-5 (1)	0.016
		Ag-Ag	6 (1)	2.86 (1)	0.011 (9)		
2.0%	One-shell	Ag-Ag	8 (1)	2.86 (1)	0.011 (2)	-1 (1)	0.021

Based on the CNs from FT-EXAFS fitting results, the possible size of Ag NCs can be estimated from ideal structure models. As shown in **Figure 4-8**, the larger particles with more silver atoms have larger CN. All three models have diameters within 2 nm. The relationship between CNs and sizes has been reported in the literature.<sup>139</sup> The 1.0 wt% Ag@Zeolite Y has a CN of 6, so the number of atoms in particles should be slightly larger than 13. The average CN of 2.0 wt% sample is 8, so the particles should have about 55 atoms.

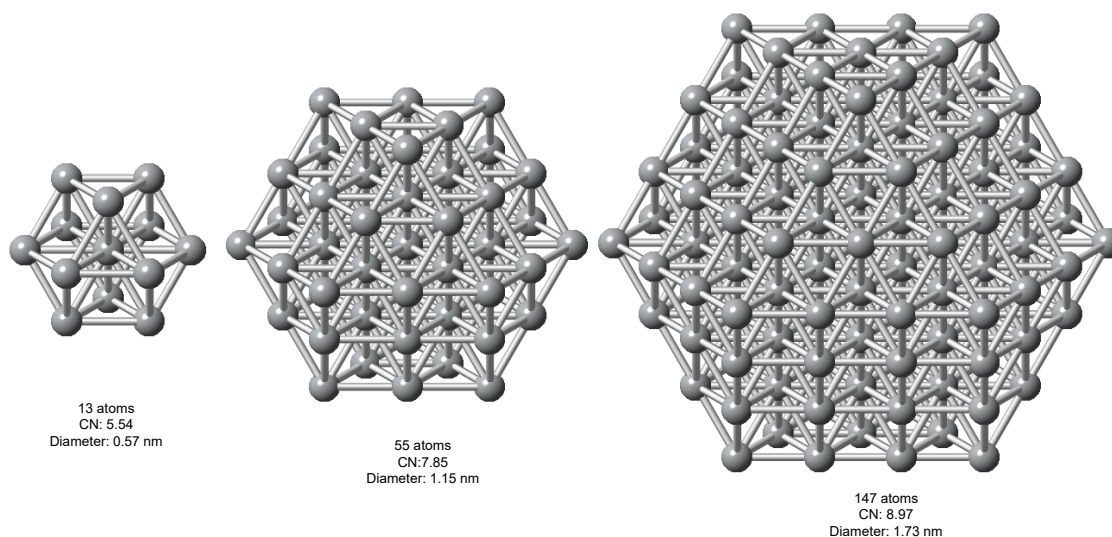


**Figure 4-8.** Crystal structures of models with different number of atoms.

#### 4.3.2 Silver Nanoclusters in Zeolite Mordenite

To further study the controlling Ag NCs by concentration of metal ions, the other series of samples, Ag NCs confined in zeolite mordenite, were prepared. The TEM images of 0.5 wt% and 2.0 wt% samples were shown in **Figure 4-9**. It is obvious that the 2.0 wt% Ag sample has a larger particle size than 0.5 wt% sample. At high concentration, some particles are on the surface zeolite, which is similar to the observation in zeolite Y samples.

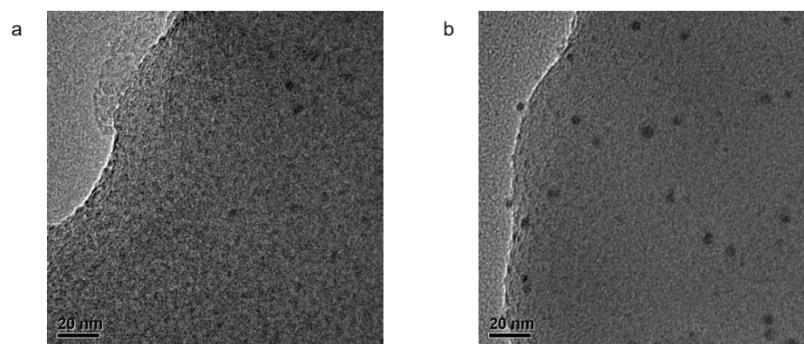


**Figure 4-9.** TEM images of a) 0.5 wt% Ag@MOR and b) 2.0 wt% Ag@MOR.

Ag K-edge XANES spectra of two samples and bulk Ag are shown in **Figure 4-10a**. The overall shape of XANES of samples is similar to that of Ag foil, suggesting the formation of metallic Ag. The spectra of samples also exhibit the oscillations with lower intensity than the spectrum of Ag foil, indicating the small size of samples. It is clearly shown that the spectra of these two Ag@MOR samples show a different feature (indicated by an arrow) from the Ag foil. This feature is more pronounced in the spectrum of 0.5 wt% sample. Meanwhile, the intensity of the peak at around 25530 eV is higher for 0.5 wt% Ag@MOR than 2.0 wt% sample. In **Figure 4-10b**, the spectra of both samples show doublet in the first peak, and it is more obvious in the spectrum of 0.5 wt% sample. These differences are due to their different coordination environment and electronic properties. The 0.5 wt% Ag@MOR may have higher oxidation state than 2.0 wt% sample. It is possible that the samples are oxidized. EXAFS analysis was performed to obtain the more detailed structural information.

**Figure 4-11** shows the FT-EXAFS spectra of samples and Ag foil. The most intense peak corresponds to a Ag-Ag shell. The same trend as Ag@Zeolite Y samples is observed; the spectrum of sample with higher concentration of silver precursor exhibits a higher peak intensity of the Ag-Ag shell, indicating large CN and particle size. This result is consistent with the TEM images. In addition, there is a small peak in the 1-2 Å range,

which is contributed from a Ag-O shell. Unlike 1.0 wt% Ag@Zeolite Y, the peak in mordenite samples appears at a lower R value, less than 2 Å. Therefore, the peak is more likely due to the oxidization of Ag NCs.

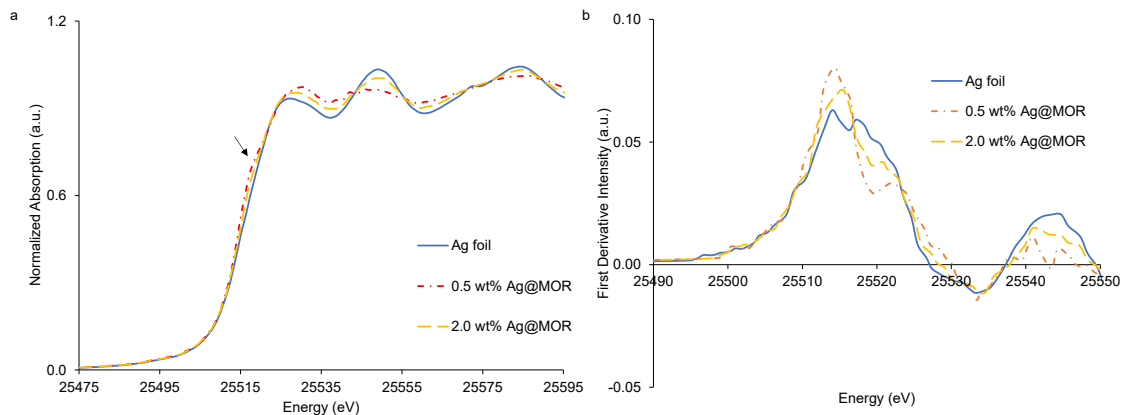


**Figure 4-10.** a) Ag K-edge XANES spectra of Ag@MOR samples and foil. b) first derivative spectra of XANES for Ag@MOR samples and foil.

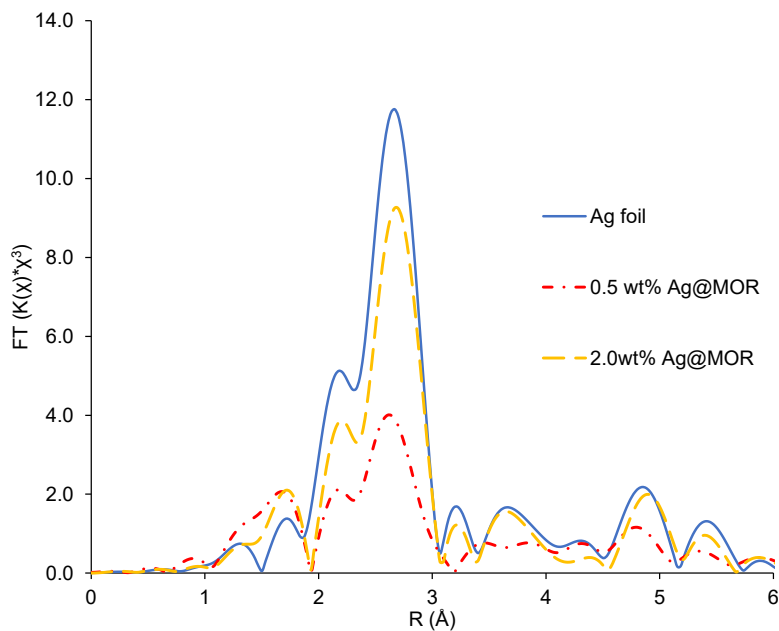


**Figure 4-11.** Ag K-edge FT-EXAFS spectra of Ag@MOR and Ag foil.

The quantitative analysis of structural information was done by fitting FT-EXAFS spectra. The spectra with fits and fitting results are demonstrated in **Figure 4-12** and **Table 4-2**. Comparing the structural parameters of Ag-Ag shell for the two samples, the

CN of the 2.0 wt% sample is larger than that of the 0.5 wt% sample, indicating large size of Ag NCs in 2.0 wt% Ag@MOR. This is in good agreement with the observation from the TEM results. As shown in **Figure 4-8**, the number of atoms in particles can be estimated from structure models. The 0.5 wt% sample with CN of 4.3 should have more than 13 atoms but less than 55 atoms. The particles in 2.0 wt% sample are much larger than particles in 0.5 wt% sample, and there should be about 147 atoms. Moreover, the 0.5 wt% sample can be fitted by two shells. The bond distances of the Ag-O shell are 2.06 Å, indicating oxidation of the Ag NCs. The contribution of the Ag-O shell peak in the 2.0 wt% sample is small compared to the contribution of the Ag-Ag shell, making it difficult to obtain a good two-shell fitting for 2.0 wt% Ag@MOR. The 0.5 wt% sample with small size of Ag NCs is less stable than the 2.0 wt% sample. It can be more easily oxidized than large particles. Combining the analysis of EXAFS and XANES, the differences in shape of XANES and first derivative spectra from the Ag foil can be considered as the features for oxidized samples. The overall trend of particle size with changing concentration of Ag ions is the same as the trend for zeolite Y samples.

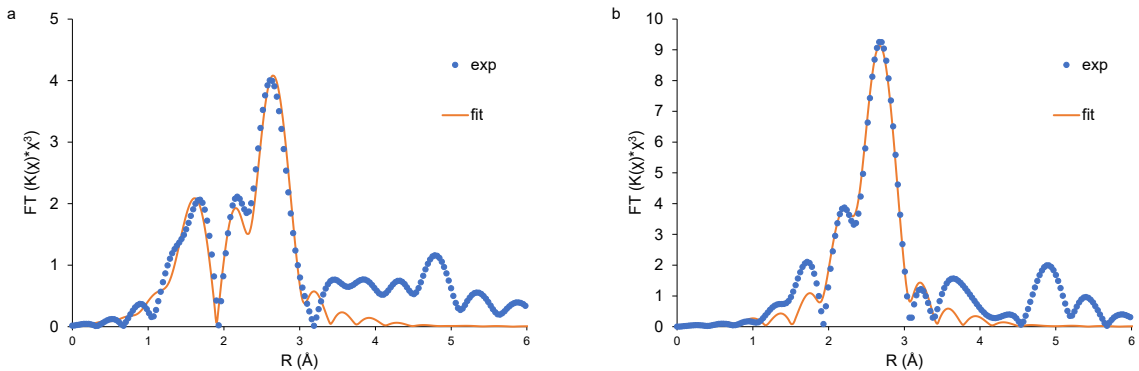


**Figure 4-12.** Fittings of FT-EXAFS spectra of a) 0.5 wt% Ag@MOR and b) 2.0 wt% Ag@MOR.



**Table 4-2.** Structural parameters of Ag@MOR as obtained from FT-EXAFS fittings.

	Shell	CN	R (Å)	$\sigma^2$ (Å <sup>2</sup> )	$\Delta E_0$ (eV)	R-factor
0.5%	Ag-O	1.1 (3)	2.06 (2)	0.003 (3)	1.0 (9)	0.013
	Ag-Ag	4.3 (6)	2.86 (1)	0.010 (1)		
2.0%	Ag-Ag	9 (1)	2.868 (7)	0.009 (1)	2.2 (8)	0.013

#### 4.3.3 Comparison of Ag Nanoclusters in Different Zeolites with Same Concentration

A close comparison of Ag NCs formed in different zeolites, but having same concentration of silver ions, was investigated. Their TEM images are shown in **Figure 4-4** and **Figure 4-9**. At low concentration, the particles in zeolite Y cannot be observed, whereas it is obvious that particles are formed in mordenite. When the concentration of Ag compound is increased to 2.0 wt%, both samples clearly show particles. The particles formed in mordenite are larger than those formed in zeolite Y. Therefore, the Ag ions tend to form larger particles in mordenite than in zeolite Y at the same concentration.

The comparison of their XANES and first derivative spectra of XANES are displayed in **Figure 4-13**. For the 0.5 wt% samples, the small peak at around 25515eV in XANES spectrum, and the doublet of first peak in the first derivative spectrum are only observed in the mordenite sample. Moreover, the sample 1.0 wt% Ag@Zeolite Y that has interactions between Ag NCs and zeolite framework does not show these special features. Therefore, only oxidized samples can exhibit these features. XANES can be used to determine the type of interactions between Ag and O. For the two 2.0 wt% samples, they have similar shape of XANES spectra. Only a small percentage of particles are oxidized in mordenite zeolite. The major difference between these two 2.0 wt% samples with different zeolites is the size of particles. The spectrum of 2.0 wt% Ag@Zeolite Y shows a narrower and more intense first peak of first derivative spectra than mordenite sample.

This observation further proves the narrowing of peak width and increase of peak intensity are related to the particle size.

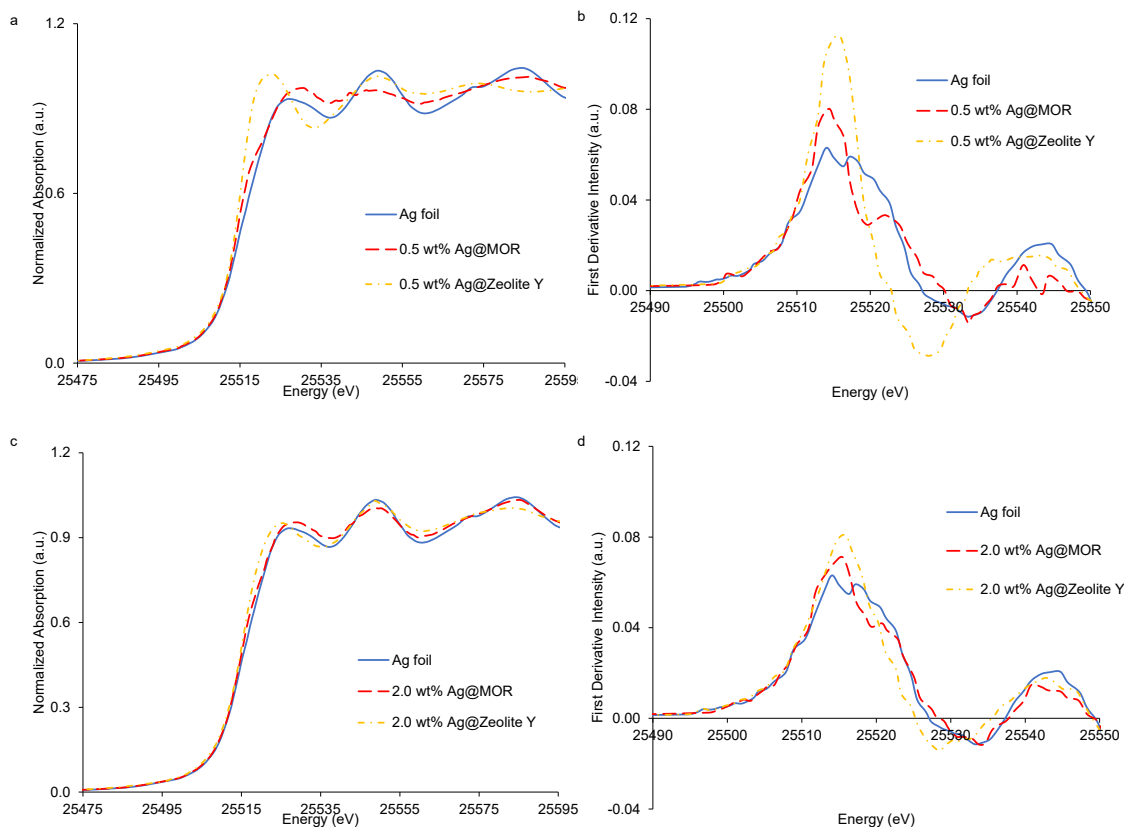


**Figure 4-13.** a) Ag K-edge XANES and b) first derivative spectra of XANE for samples at 0.5 wt% and foil. c) Ag K-edge XANES and d) first derivative spectra of XANE for samples at 2.0 wt% and foil.

Their FT-EXAFS spectra are compared as shown in **Figure 4-14** and the fitting results of the 2.0 wt% samples are summarized in **Table 4-3**. For both concentrations, the peak intensity of the Ag-Ag shell is higher for Ag NCs formed in mordenite than those in zeolite Y. From the fitting results, 2.0 wt% Ag@MOR has a slightly larger CN than 2.0 wt% Ag@Zeolite Y. These observations indicate the Ag NCs with larger size are formed in mordenite. The possible explanation is that the available exchange sites are different in these two zeolites.<sup>140</sup> Moreover, the ability of exchange of cations for Ag ions in MOR are greater than zeolite Y.<sup>141,142</sup> When the concentrations of metal ions are the same for

both zeolites, more Ag ions are likely loaded into MOR than zeolite Y. So, the particles in MOR are larger. In addition, the Ag-O shell is more pronounced for mordenite samples. These differences could be explained by the structure of zeolites, as shown in **Figure 4-14c.d**. Mordenite has two-dimensional channels of 6.5 x 7.0 Å, and zeolite Y has 3D 12-membered ring channels about 7.4 Å.<sup>140,143</sup> Ag NCs in 2D channels are less well protected than particles in 3D channels, so they can immigrate easily and form large particles. For the 2D channels, the possibility of particles exposure on surface is large, resulting in a higher chance to be oxidized. Therefore, Ag NCs in mordenite tend to have large particle size and they are more easily oxidized than NCs in zeolite Y. Ag NCs in zeolite Y are well protected, and they can have interactions with the zeolite framework. Therefore, zeolite Y shows a better ability to confine Ag NCs. Due to the differences in size and surface interactions, these Ag NCs show different atomic structure and electronic properties.

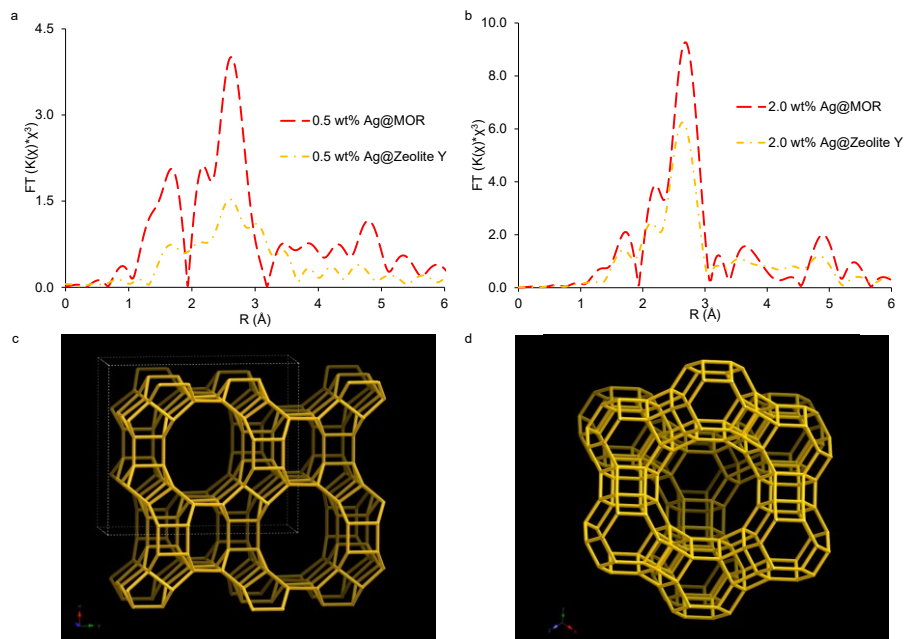


**Figure 4-14.** Ag K-edge FT-EXAFS spectra of samples and Ag foil at a) 0.5 wt% and b) 2.0 wt%. Structure of c) mordenite and d) zeolite Y.

**Table 4-3.** Structural parameters of 2.0wt% samples as obtained from FT-EXAFS fittings.

	Shell	CN	R (Å)	$\sigma^2$ (Å <sup>2</sup> )	$\Delta E_0$ (eV)	R-factor
2.0% Ag@Zeolite Y	Ag-Ag	8 (1)	2.86 (1)	0.011 (2)	-1 (1)	0.021
2.0% Ag@MOR	Ag-Ag	9 (1)	2.868 (7)	0.009 (1)	2.2 (8)	0.013

#### 4.3.4 Catalytic Reaction of 1.0 wt% Ag@Zeolite Y

Among these Ag NC samples, 1.0 wt% Ag@Zeolite Y shows the most even distribution in zeolite from TEM. From XAS analysis, it is the only sample that shows the interactions between Ag NCs and zeolites framework. A preliminary study of catalytic reaction was performed for 1.0 wt% Ag@Zeolite Y. The oxidation of styrene reaction was carried out to test the catalytic activity of the sample. Based on the analysis of NMR data, the peaks of styrene were disappeared after 10 hours, indicating the reaction was completed after 10 hours by using 1.0 wt% Ag@Zeolite Y as a catalyst. Compared with the similar material under the same reaction conditions, the conversion rate of 0.01g Ag-based 4A zeolite is 40.1% after 24 hours.<sup>144</sup> Thus, 1.0 wt% Ag@Zeolite Y shows promising catalytic activities for styrene oxidation. The differences in catalytic activities between our catalyst and literature catalysts could be explained by the size of particles. The Ag-based 4A zeolite has particles in size from 17 to 35 nm, which are larger than the size of Ag@Zeolite Y. The small size of NCs can provide more surface sites for the catalytic reaction, which are beneficial for the oxidation of styrene reaction. Moreover, Ag-based 4A zeolite used in the literature showed some particles on the surface of zeolite frameworks. In contrast, most particles in 1.0 wt% Ag@Zeolite Y sample are well confined in zeolite and they have interactions with zeolite frameworks. The surface atomic structure and electronic properties are altered. The catalytic activities

may be affected by these interactions. It is possible that the zeolite Y have synergistic effect with Ag NCs to improve the catalytic activities. Unfortunately, the control experiment and tests of other samples could not be done due to the pandemic situation. Further studies on their catalytic properties should be done in the future. The interactions between zeolites and Ag NCs may have negative effect on the catalytic activities. When the surface atoms have interactions with oxygen in frameworks, the number of available surface sites decreases. Although we could not test the catalytic activities of all samples, our catalyst shows promising activities. The Ag NCs confined in zeolites have potentials to be high performance catalysts.

#### **4.4 Summary**

To summarize, Ag NCs confined in zeolites were successfully synthesized by using the ion-exchange method followed by reduction. There are two ways to control the particles size: adjusting the concentration of metal ions and selecting the types of zeolite. Both the TEM and XAS results show that, for the same zeolite, the sample with high concentration of Ag ions tend to have higher CNs, indicating larger particle sizes. For low concentration samples, small changes in concentration do not cause obvious differences in structure and particle sizes. At the same concentration, Ag@MOR tend to have larger particles than Ag@Zeolite Y due to their differences in zeolite structure. Zeolite Y with 3D channels show a better ability to confine small Ag NCs than mordenite with 2D channels. From XANES spectra analysis, the intensity of the first peak following the absorption edge increases as the concentration of Ag ions decreases, indicating the changes of electronic properties. The XANES spectrum of oxidized Ag NCs shows a special feature in XANES spectra and its first derivative spectrum has a

doublet in low energy region, which could be used as a fingerprint to identify the oxidized Ag species. By analysis of FT-EXAFS, 1.0 wt% Ag@Zeolite Y shows the interactions between NCs and the zeolite frameworks. Thus, two possible types of Ag-O bonds can be found in Ag NCs confined in zeolites. XAS is a good tool to distinguish whether the surface Ag-O bonds in the sample are due to the oxidation or the interactions between NCs and zeolites framework. Finally, the preliminary test of catalytic activity was done for 1.0 wt% Ag@Zeolite Y. The reaction catalyzed by our 1.0 wt% Ag@Zeolite Y was completed within much shorter time than the literature reference. This promising catalytic activity together with their controllable structure and electronic properties suggest these Ag NCs could be excellent candidates for catalytic applications.

## Chapter 5 - Conclusions and Future Work

### 5.1 Conclusions

In the study of ligand-protected Ag NCs, the electronic and bonding properties of Ag<sub>25</sub> were investigated by using X-ray spectroscopies. Based on the published structure model of Ag<sub>25</sub>, a detailed study was carried out from site-specific perspective. A unique XPS data analysis method was developed to probe the electronic properties of center, surface and staple sites. The final state effect on XPS binding energy shift can be excluded when the central atom was used as reference. Compared with its counterpart of Au<sub>25</sub> in Au NCs, Ag atoms in the staple and surface of Ag<sub>25</sub> show different charge transfer behavior from Au atoms in the same sites of Au<sub>25</sub>. More electrons are withdrawn by thiolate ligands in Ag<sub>25</sub> than in Au<sub>25</sub>. Moreover, the site-specific simulations of XANES spectra show that the Ag<sub>2</sub>S<sub>3</sub> staple motifs have a large impact on the electronic properties of the Ag<sub>25</sub> cluster. Furthermore, Ag<sub>25</sub> exhibit unique temperature-dependent bonding properties by analysis of FT-EXAFS. Comparing with Au<sub>25</sub>, it shows more molecular-like behavior when the temperature changes. The site-specific analysis of electronic and bonding properties of Ag<sub>25</sub> offers an in-depth understanding of structure-property relationship, and might be useful to guide their potential applications.

In addition to ligand-protected NCs, Ag NCs confined in zeolites were successfully synthesized by using ion-exchange method followed by reduction. TEM and XAS results show that both concentrations of metals and types of zeolites can be used to control the size and structure of Ag NCs. When the same zeolites are used, the cluster sizes increase with the Ag concentration. At the same concentration, larger clusters are more likely formed in Ag@MOR than Ag@Zeolite Y because of differences in zeolite

structures. XANES spectrum has been demonstrated as a good fingerprint to determine the origins of Ag NCs surface bonds. Ag NCs confined within zeolite Y with 1.0 wt% was found to show the interactions between the cluster surface and zeolite framework. For Ag@MOR, the surface of Ag NCs is more likely to be oxidized. The XANES spectra of these oxidized Ag NCs samples show a small peak feature at around the edge, and their first peak in first derivative spectra exhibit a doublet. The electronic properties of these Ag NCs were found to be different because of the differences shown in XANES spectra. Finally, the sample with 1.0 wt% Ag confined within zeolite Y was used for catalytic study in oxidation of styrene. In comparison with similar Ag nanomaterials, the Ag-based 4A zeolite catalyst used in the literature exhibited 40.1% conversion rate after 24 hours, but the reaction catalyzed by 1.0 wt% Ag@Zeolite Y was completed after 10 hours. These preliminary catalytic results, together with the controllable surface and electronic properties of Ag NCs observed in this work, imply that these zeolite-supported NCs might be used as promising candidates for various catalytic applications.

## **5.2 Future work**

The study of Ag<sub>25</sub> shows unique electronic and bonding properties from its counterpart Au<sub>25</sub>. Some studies showed that Au<sub>25</sub> has good catalytic activities. Since Ag<sub>25</sub> is the only match analogues with Au<sub>25</sub>, it could be potentially good catalysts as well. The catalytic activities of Ag<sub>25</sub> can be tested and compared with Au<sub>25</sub> in the future. Moreover, it was found that the doping on Ag<sub>25</sub> can enhance the photoluminescence, but the reasons for enhancement are not clear. In the future, the bonding and electronic properties of doped Ag<sub>25</sub> such as AuAg<sub>24</sub>, PtAg<sub>24</sub> can be investigated by XAS. The site-specific



analysis method may help give explanations for the enhancement of photoluminescence and their catalytic activities.

In the study of Ag NCs confined in zeolite, only a preliminary test was done on the catalytic activity. Further study on the catalytic activities should be carried out. The activities of zeolites without Ag NCs should be tested as comparison reference. It is possible that the zeolites also have catalytic activities for styrene oxidation. With this control experiment, all peaks in NMR spectrum can be identified. The other samples with different concentrations of Ag ions and types of zeolites should be tested as well to find the optimized synthetic conditions. In order to have reliable catalytic results, an appropriate internal standard should be selected for NMR measurements. Same amount of internal standard with known concentration should be added. Then, the conversion rate of catalytic reaction can be obtained based on the peak integral from NMR spectrum. Moreover, the porous structure of zeolites should have effect on selectivity. In the future study, the selectivity of these small Ag NCs in catalytic reaction can be investigated.

## References

- [1] Vert, M.; Doi, Y.; Hellwich, K. H.; Hess, M.; Hodge, P.; Kubisa, P.; Rinaudo, M.; Schué, F. *Pure Appl. Chem.* **2012**, *84*, 377.
- [2] Chen, G.; Roy, I.; Yang, C.; Prasad, P. N. *Chem. Rev.* **2016**, *116*, 2826.
- [3] Burda, C.; Chen, X.; Narayanan, R.; El-Sayed, M. A. *Chem. Rev.* **2005**, *105*, 1025.
- [4] Okuyama, K.; Lenggoro, W. W. *Chem. Eng. Sci.* **2003**, *58*, 537.
- [5] Anu Mary Ealia, S.; Saravanakumar, M. P. *IOP Conf. Ser. Mater. Sci. Eng.* **2017**, *263*, 032019.
- [6] Pareek, V.; Bhargava, A.; Gupta, R.; Jain, N.; Panwar, J. *Adv. Sci. Eng. Med.* **2017**, *9*, 527.
- [7] Doria, G.; Conde, J.; Veigas, B.; Giestas, L.; Almeida, C.; Assunção, M.; Rosa, J.; Baptista, P. V. *Sensors* **2012**, *12*, 1657.
- [8] Rodrigues, T. S.; Da Silva, A. G. M.; Camargo, P. H. C. *J. Mater. Chem. A* **2019**, *7*, 5857.
- [9] Jain, P. K.; Huang, X.; El-Sayed, I. H.; El-Sayed, M. A. *Plasmonics* **2007**, *2*, 107.
- [10] Li, H.; Rothberg, L. J. *J. Am. Chem. Soc.* **2004**, *126*, 10958.
- [11] Ding, X.; Yuan, P.; Gao, N.; Zhu, H.; Yang, Y. Y.; Xu, Q. H. *Nanomedicine Nanotechnology, Biol. Med.* **2017**, *13*, 297.
- [12] Suchomel, P.; Kvitek, L.; Pucek, R.; Panacek, A.; Halder, A.; Vajda, S.; Zboril, R. *Sci. Rep.* **2018**, *8*, 4589.
- [13] Narayanan, R.; El-Sayed, M. A. *Nano Lett.* **2004**, *4*, 1343.
- [14] Yamamoto, T. A.; Nakagawa, T.; Seino, S.; Nitani, H. *Appl. Catal. A Gen.* **2010**, *387*, 195.
- [15] Natsuki, J. *Int. J. Mater. Sci. Appl.* **2015**, *4*, 325.
- [16] Rai, M.; Yadav, A.; Gade, A. *Biotechnol. Adv.* **2009**, *27*, 76.
- [17] Alexander, J. W. *Surg. Infect. (Larchmt)*. **2009**, *10*, 289.
- [18] Kim, J. S.; Kuk, E.; Yu, K. N.; Kim, J. H.; Park, S. J.; Lee, H. J.; Kim, S. H.; Park, Y. K.; Park, Y. H.; Hwang, C. Y.; Kim, Y. K.; Lee, Y. S.; Jeong, D. H.; Cho, M. H. *Nanomedicine Nanotechnology, Biol. Med.* **2007**, *3*, 95.
- [19] Ueda, J.; Samusawa, M.; Kumagai, K.; Ishida, A.; Tanabe, S. *J. Mater. Sci.* **2014**, *49*, 3299.
- [20] Fabrega, J.; Luoma, S. N.; Tyler, C. R.; Galloway, T. S.; Lead, J. R. *Environ. Int.* **2011**, *37*, 517.

- [21] Haider, A.; Kang, I. K. *Adv. Mater. Sci. Eng.* **2015**, *2015*, DOI 10.1155/2015/165257.
- [22] Ip, M.; Lui, S. L.; Poon, V. K. M.; Lung, I.; Burd, A. *J. Med. Microbiol.* **2006**, *55*, 59.
- [23] Padmos, J. D.; Boudreau, R. T. M.; Weaver, D. F.; Zhang, P. *Langmuir* **2015**, *31*, 3745.
- [24] Li, H.; Xu, D. *TrAC - Trends Anal. Chem.* **2014**, *61*, 67.
- [25] McFarland, A. D.; Van Duyne, R. P. *Nano Lett.* **2003**, *3*, 1057.
- [26] Fan, M.; Brolo, A. G. *Phys. Chem. Chem. Phys.* **2009**, *11*, 7381.
- [27] Srichan, C.; Ekpanyapong, M.; Horprathum, M.; Eiamchai, P.; Nuntawong, N.; Phokharatkul, D.; Danvirutai, P.; Bohez, E.; Wisitsoraat, A.; Tuantranont, A. *Sci. Rep.* **2016**, *6*, 1.
- [28] Vidhu, V. K.; Philip, D. *Micron* **2014**, *56*, 54.
- [29] Mallick, K.; Witcomb, M.; Scurrrell, M. *Mater. Chem. Phys.* **2006**, *97*, 283.
- [30] Zhao, X. H.; Li, Q.; Ma, X. M.; Xiong, Z.; Quan, F. Y.; Xia, Y. Z. *RSC Adv.* **2015**, *5*, 49534.
- [31] Xu, R.; Wang, D.; Zhang, J.; Li, Y. *Chem. Asian J.* **2006**, *1*, 888.
- [32] Chimentão, R. J.; Kirm, I.; Medina, F.; Rodríguez, X.; Cesteros, Y.; Salagre, P.; Sueiras, J. E.; Fierro, J. L. G. *Appl. Surf. Sci.* **2005**, *252*, 793.
- [33] Aiken, J. D.; Finke, R. G. *J. Mol. Catal. A Chem.* **1999**, *145*, 1.
- [34] Zhang, L.; Wang, E. *Nano Today* **2014**, *9*, 132.
- [35] Díez, I.; Ras, R. H. A. *Nanoscale* **2011**, *3*, 1963.
- [36] Wilcoxon, J. P.; Abrams, B. L. *Chem. Soc. Rev.* **2006**, *35*, 1162.
- [37] Díez, I.; Pusa, M.; Kulmala, S.; Jiang, H.; Walther, A.; Goldmann, A. S.; Müller, A. H. E.; Ikkala, O.; Ras, R. H. A. *Angew. Chemie - Int. Ed.* **2009**, *48*, 2122.
- [38] Shang, L.; Dong, S. *Chem. Commun.* **2008**, 1088.
- [39] Padmos, J. D.; Boudreau, R. T. M.; Weaver, D. F.; Zhang, P. *J. Phys. Chem. C* **2015**, *119*, 24627.
- [40] Yuan, X.; Tay, Y.; Dou, X.; Luo, Z.; Leong, D. T.; Xie, J. *Anal. Chem.* **2013**, *85*, 1913.
- [41] Kumar, S.; Bolan, M. D.; Bigioni, T. P. *J. Am. Chem. Soc.* **2010**, *132*, 13141.
- [42] AbdulHalim, L. G.; Bootharaju, M. S.; Tang, Q.; Del Gobbo, S.; AbdulHalim, R. G.; Eddaoudi, M.; Jiang, D. E.; Bakr, O. M. *J. Am. Chem. Soc.* **2015**, *137*, 11970.

- [43] Savic, S.; Vojisavljevic, K.; Počuča-Nešić, M.; Zivojevic, K.; Mladenovic, M.; Knezevic, N. *Metall. Mater. Eng.* **2018**, *24*, 225.
- [44] Mazzitelli, C. L.; Brodbelt, J. S. *J. Am. Soc. Mass Spectrom.* **2006**, *17*, 676.
- [45] Jin, R.; Zhao, S.; Xing, Y.; Jin, R. *CrystEngComm* **2016**, *18*, 3996.
- [46] Zheng, K.; Yuan, X.; Goswami, N.; Zhang, Q.; Xie, J. *RSC Adv.* **2014**, *4*, 60581.
- [47] Desiredy, A.; Conn, B. E.; Guo, J.; Yoon, B.; Barnett, R. N.; Monahan, B. M.; Kirschbaum, K.; Griffith, W. P.; Whetten, R. L.; Landman, U.; Bigioni, T. P. *Nature* **2013**, *501*, 399.
- [48] Häkkinen, H. *Chem. Soc. Rev.* **2008**, *37*, 1847.
- [49] Walter, M.; Akola, J.; Lopez-Acevedo, O.; Jadzinsky, P. D.; Calero, G.; Ackerson, C. J.; Whetten, R. L.; Gronbeck, H.; Hakkinen, H. *Proc. Natl. Acad. Sci.* **2008**, *105*, 9157.
- [50] Chakraborty, I.; Udayabhaskararao, T.; Deepesh, G. K.; Pradeep, T. *J. Mater. Chem. B* **2013**, *1*, 4059.
- [51] Le Guével, X.; Spies, C.; Daum, N.; Jung, G.; Schneider, M. *Nano Res.* **2012**, *5*, 379.
- [52] Auerbach, S.; Carrado, K.; Dutta, P.; Lobo, R. in *Handb. Zeolite Sci. Technol.*, **2003**.
- [53] Majsztrik, P. W. *Appl. Evol. Comput. Chem.* **2008**, *141*, 235.
- [54] Andrieux-Ledier, A.; Tremblay, B.; Courty, A. *J. Phys. Chem. C* **2013**, *117*, 14850.
- [55] Luo, C.; Zhang, Y.; Zeng, X.; Zeng, Y.; Wang, Y. *J. Colloid Interface Sci.* **2005**, *288*, 444.
- [56] Verma, V. C.; Kharwar, R. N.; Gange, A. C. *Nanomedicine* **2010**, *5*, 33.
- [57] Singh, R.; Shedbalkar, U. U.; Wadhvani, S. A.; Chopade, B. A. *Appl. Microbiol. Biotechnol.* **2015**, *99*, 4579.
- [58] Xie, Y.; Kocaefer, D.; Chen, C.; Kocaefer, Y. *J. Nanomater.* **2016**, *2016*, DOI 10.1155/2016/2302595.
- [59] Udayabhaskararao, T.; Pradeep, T. *J. Phys. Chem. Lett.* **2013**, *4*, 1553.
- [60] Dhanalakshmi, L.; Udayabhaskararao, T.; Pradeep, T. *Chem. Commun.* **2012**, *48*, 859.
- [61] Chakraborty, I.; Udayabhaskararao, T.; Pradeep, T. *Chem. Commun.* **2012**, *48*, 6788.
- [62] Chakraborty, I.; Govindarajan, A.; Erusappan, J.; Ghosh, A.; Pradeep, T.; Yoon, B.; Whetten, R. L.; Landman, U. *Nano Lett.* **2012**, *12*, 5861.
- [63] Udayabhaskararao, T.; Bootharaju, M. S.; Pradeep, T. *Nanoscale* **2013**, *5*, 9404.
- [64] Joshi, C. P.; Bootharaju, M. S.; Alhilaly, M. J.; Bakr, O. M. *J. Am. Chem. Soc.* **2015**, *137*,

11578.

- [65] Farrusseng, D.; Tuel, A. *New J. Chem.* **2016**, *40*, 3933.
- [66] Wang, N.; Sun, Q.; Yu, J. *Adv. Mater.* **2019**, *31*, 1803966.
- [67] Davis, R. J. *J. Catal.* **2003**, *216*, 396.
- [68] Armor, J. N. *Microporous Mesoporous Mater.* **1998**, *22*, 451.
- [69] Chai, Y.; Shang, W.; Li, W.; Wu, G.; Dai, W.; Guan, N.; Li, L. *Adv. Sci.* **2019**, *6*, 1900299.
- [70] Caciuffo, R.; Melone, S.; Rustichelli, F.; Boeuf, A. *Phys. Rep.* **1987**, *152*, 1.
- [71] Lea, K. R. *Phys. Rep.* **1978**, *43*, 337.
- [72] van der Linden, M.; van Bunningen, A. J.; Amidani, L.; Bransen, M.; Elnaggar, H.; Glatzel, P.; Meijerink, A.; F de Groot, F. M. *ACS Nano* **2018**, *12*, 55.
- [73] Sham, T. K. *Int. J. Nanotechnol.* **2008**, *5*, 1194.
- [74] Schroeder, S. L. M.; Moggridge, G. D.; Rayment, T.; Lambert, R. M. *J. Mol. Catal. A Chem.* **1997**, *119*, 357.
- [75] Nelson, R. C.; Miller, J. T. *Catal. Sci. Technol* **2012**, *2*, 461.
- [76] Zhang, P. *J. Phys. Chem. C* **2014**, *118*, 25291.
- [77] Duchesne, P. N.; Chen, G.; Zheng, N.; Zhang, P. *J. Phys. Chem. C* **2013**, *117*, 26324.
- [78] Funke, H.; Scheinost, A. C.; Chukalina, M. *Phys. Rev. B* **2005**, *71*, 094110.
- [79] Chevrier, D. M.; Raich, L.; Rovira, C.; Das, A.; Luo, Z.; Yao, Q.; Chatt, A.; Xie, J.; Jin, R.; Akola, J.; Zhang, P. *J. Am. Chem. Soc.* **2018**, *140*, 15430.
- [80] Duchesne, P. N.; Li, Z. Y.; Deming, C. P.; Fung, V.; Zhao, X.; Yuan, J.; Regier, T.; Aldalbahi, A.; Almarhoon, Z.; Chen, S.; Jiang, D. en; Zheng, N.; Zhang, P. *Nat. Mater.* **2018**, *17*, 1033.
- [81] Ankudinov, A.; Ravel, B. *Phys. Rev. B - Condens. Matter Mater. Phys.* **1998**, *58*, 7565.
- [82] Fadley, C. S. *J. Electron Spectros. Relat. Phenomena* **2010**, *178–179*, 2.
- [83] Peters, S.; Peredkov, S.; Neeb, M.; Eberhardt, W.; Al-Hada, M. *Surf. Sci.* **2013**, *608*, 129.
- [84] Yang, D. Q.; Sacher, E. *Appl. Surf. Sci.* **2002**, *195*, 187.
- [85] Zhang, P.; Sham, T. K. *Phys. Rev. Lett.* **2003**, *90*, 4.
- [86] Moriarty, P. *Phys. Rev. Lett.* **2004**, *92*, 109601.

- [87] Wertheim, G. K.; Dicenzo, S. B.; Buchanan, D. N. E. *Phys. Rev. B* **1986**, *33*, 5384.
- [88] Hufner, S.; Wertheim, G. K.; Wernick, J. H. *Phys. Rev. B* **1973**, *8*, 4511.
- [89] McFeely, F. R.; Stöhr, J.; Apai, G.; Wehner, P. S.; Shirley, D. A. *Phys. Rev. B* **1976**, *14*, 3273.
- [90] Apai, G.; Lee, S. T.; Mason, M. G. *Solid State Commun.* **1981**, *37*, 213.
- [91] Fang, J.; Zhang, B.; Yao, Q.; Yang, Y.; Xie, J.; Yan, N. *Coord. Chem. Rev.* **2016**, *322*, 1.
- [92] Du, Y.; Sheng, H.; Astruc, D.; Zhu, M. *Chem. Rev.* **2020**, *120*, 526.
- [93] Li, G.; Jin, R. *Acc. Chem. Res.* **2013**, *46*, 1749.
- [94] Wong, O. A.; Hansen, R. J.; Ni, T. W.; Heinecke, C. L.; Compel, W. S.; Gustafson, D. L.; Ackerson, C. J. *Nanoscale* **2013**, *5*, 10525.
- [95] Katla, S. K.; Zhang, J.; Castro, E.; Bernal, R. A.; Li, X. *ACS Appl. Mater. Interfaces* **2018**, *10*, 75.
- [96] Zhang, X.-D.; Chen, J.; Luo, Z.; Wu, D.; Shen, X.; Song, S.-S.; Sun, Y.-M.; Liu, P.-X.; Zhao, J.; Huo, S.; Fan, S.; Fan, F.; Liang, X.-J.; Xie, J. *Adv. Healthc. Mater.* **2014**, *3*, 133.
- [97] Zhu, Y.; Qian, H.; Zhu, M.; Jin, R. *Adv. Mater.* **2010**, *22*, 1915.
- [98] Kauffman, D. R.; Alfonso, D.; Matranga, C.; Ohodnicki, P.; Deng, X.; Siva, R. C.; Zeng, C.; Jin, R. *Chem. Sci.* **2014**, *5*, 3151.
- [99] Yu, C.; Li, G.; Kumar, S.; Kawasaki, H.; Jin, R. *J. Phys. Chem. Lett.* **2013**, *4*, 2847.
- [100] Jin, R.; Zeng, C.; Zhou, M.; Chen, Y. *Chem. Rev.* **2016**, *116*, 10346.
- [101] Weerawardene, K. L. D. M.; Aikens, C. M. *J. Phys. Chem. C* **2018**, *122*, 2440.
- [102] Veselska, O.; Dessal, C.; Melizi, S.; Guillou, N.; Podbevšek, D.; Ledoux, G.; Elkaim, E.; Fateeva, A.; Demessence, A. *Inorg. Chem.* **2019**, *58*, 99.
- [103] MacDonald, M. A.; Chevrier, D. M.; Zhang, P.; Qian, H.; Jin, R. *J. Phys. Chem. C* **2011**, *115*, 15282.
- [104] Yang, R.; Morris, D. J.; Higaki, T.; Ward, M. J.; Jin, R.; Zhang, P. *ACS Omega* **2018**, *3*, 14981.
- [105] Walsh, A. G.; Chen, Z.; Zhang, P. *J. Phys. Chem. C* **2020**, *124*, 4339.
- [106] Zhu, M.; Lanni, E.; Garg, N.; Bier, M. E.; Jin, R. *J. Am. Chem. Soc.* **2008**, *130*, 1138.
- [107] *CasaXPS Manual 2 . 3 . 15 CasaXPS Processing Software for XPS Spectra*, **2009**.
- [108] Christensen, S. L.; MacDonald, M. A.; Chatt, A.; Zhang, P.; Qian, H.; Jin, R. *J. Phys. Chem. C* **2012**, *116*, 26932.

- [109] Ravel, B.; Newville, M. *J. Synchrotron Radiat.* **2005**, *12*, 537.
- [110] Visikovskiy, A.; Matsumoto, H.; Mitsuhashi, K.; Nakada, T.; Akita, T.; Kido, Y. *Phys. Rev. B* **2011**, *83*, 165428.
- [111] Zhu, M.; Aikens, C. M.; Hollander, F. J.; Schatz, G. C.; Jin, R. *J. Am. Chem. Soc.* **2008**, *130*, 5883.
- [112] Heaven, M. W.; Dass, A.; White, P. S.; Holt, K. M.; Murray, R. W. *J. Am. Chem. Soc.* **2008**, *130*, 3754.
- [113] Ashwell, A. P.; Ratner, M. A.; Schatz, G. C. *Adv. Quantum Chem.* **2017**, *75*, 117.
- [114] Juarez-Mosqueda, R.; Mpourmpakis, G. *Phys. Chem. Chem. Phys.* **2019**, *21*, 22272.
- [115] Häkkinen, H.; Moseler, M.; Landman, U. *Phys. Rev. Lett.* **2002**, *89*, 033401.
- [116] Zhang, B.; Safonova, O. V.; Pollitt, S.; Salassa, G.; Sels, A.; Kazan, R.; Wang, Y.; Rupprechter, G.; Barrabés, N.; Bürgi, T. *Phys. Chem. Chem. Phys.* **2018**, *20*, 5312.
- [117] Zhang, T.; Chen, Z.; Walsh, A. G.; Li, Y.; Zhang, P. *Adv. Mater.* **2020**, *32*, 2002910.
- [118] Hansen, T. W.; Delariva, A. T.; Challa, S. R.; Datye, A. K. *Acc. Chem. Res.* **2013**, *46*, 1720.
- [119] Challa, S. R.; Delariva, A. T.; Hansen, T. W.; Helveg, S.; Sehested, J.; Hansen, P. L.; Garzon, F.; Datye, A. K. *J. Am. Chem. Soc.* **2011**, *133*, 20672.
- [120] Harada, T.; Ikeda, S.; Ng, Y. H.; Sakata, T.; Mori, H.; Torimoto, T.; Matsumura, M. *Adv. Funct. Mater.* **2008**, *18*, 2190.
- [121] Rebelli, J.; Rodriguez, A. A.; Ma, S.; Williams, C. T.; Monnier, J. R. *Catal. Today* **2011**, *160*, 170.
- [122] Yang, X.; Sun, J. K.; Kitta, M.; Pang, H.; Xu, Q. *Nat. Catal.* **2018**, *1*, 214.
- [123] Gurin, V. S.; Petranovskii, V. P.; Hernandez, M. A.; Bogdanchikova, N. E.; Alexeenko, A. A. *Mater. Sci. Eng. A* **2005**, *391*, 71.
- [124] Cruciani, G. *J. Phys. Chem. Solids* **2006**, *67*, 1973.
- [125] Sun, Q.; Wang, N.; Bai, R.; Hui, Y.; Zhang, T.; Do, D. A.; Zhang, P.; Song, L.; Miao, S.; Yu, J. *Adv. Sci.* **2019**, *6*, 1802350.
- [126] Choi, M.; Wu, Z.; Iglesia, E. *J. Am. Chem. Soc.* **2010**, *132*, 9129.
- [127] Zhang, Y.; Chen, F.; Zhuang, J.; Tang, Y.; Wang, D.; Wang, Y.; Dong, A.; Ren, N. *Chem. Commun.* **2002**, *2*, 2814.
- [128] Zhang, W.; Qiao, X.; Chen, J. *Mater. Sci. Eng. B Solid-State Mater. Adv. Technol.* **2007**, *142*, 1.

- [129] Sun, T.; Seff, K. *Chem. Rev.* **1994**, *94*, 857.
- [130] Mondale, K. D.; Carland, R. M.; Aplan, F. F. *Miner. Eng.* **1995**, *8*, 535.
- [131] Liu, F.; Wechsler, D.; Zhang, P. *Chem. Phys. Lett.* **2008**, *461*, 254.
- [132] Otto, T.; Ramallo-López, J. M.; Giovanetti, L. J.; Requejo, F. G.; Zones, S. I.; Iglesia, E. *J. Catal.* **2016**, *342*, 125.
- [133] Inglezakis, V. J. *J. Colloid Interface Sci.* **2005**, *281*, 68.
- [134] Huwe, H.; Fröba, M. *Carbon* **2007**, *45*, 304.
- [135] Talebi, J.; Halladj, R.; Askari, S. *J. Mater. Sci.* **2010**, *45*, 3318.
- [136] Ahmad, A.; Mukherjee, P.; Senapati, S.; Mandal, D.; Khan, M. I.; Kumar, R.; Sastry, M. *Colloids Surfaces B Biointerfaces* **2003**, *28*, 313.
- [137] Shamel, K.; Ahmad, M. Bin; Zargar, M.; Yunus, W. M. Z. W.; Ibrahim, N. A. *Int. J. Nanomedicine* **2011**, *6*, 331.
- [138] Tang, S.; Wu, W.; Yu, J. *Phys. Chem. Chem. Phys.* **2016**, *18*, 7797.
- [139] Liu, F.; Zhang, P. *Appl. Phys. Lett.* **2010**, *96*, 43105.
- [140] Chen, J. H.; Lin, J. N.; Kang, Y. M.; Yu, W. Y.; Kuo, C. N.; Wan, B. Z. *Appl. Catal. A Gen.* **2005**, *291*, 162.
- [141] Fletcher, P.; Townsend, R. P. *J. Chromatogr. A* **1980**, *201*, 93.
- [142] Fletcher, P.; Townsend, R. P. *J. Chem. Soc. Faraday Trans. 1* **1981**, *77*, 497.
- [143] Klinowski, J.; Ramdas, S.; Thomas, J. M.; Fyfe, C. A.; Hartman, J. S. *J. Chem. Soc. Faraday Trans. 2* **1982**, *78*, 1025.
- [144] Hu, X.; Bai, J.; Li, C.; Liang, H.; Sun, W. *Eur. J. Inorg. Chem.* **2015**, *2015*, 3758.



## Appendix A – Supporting Information for Chapter 3

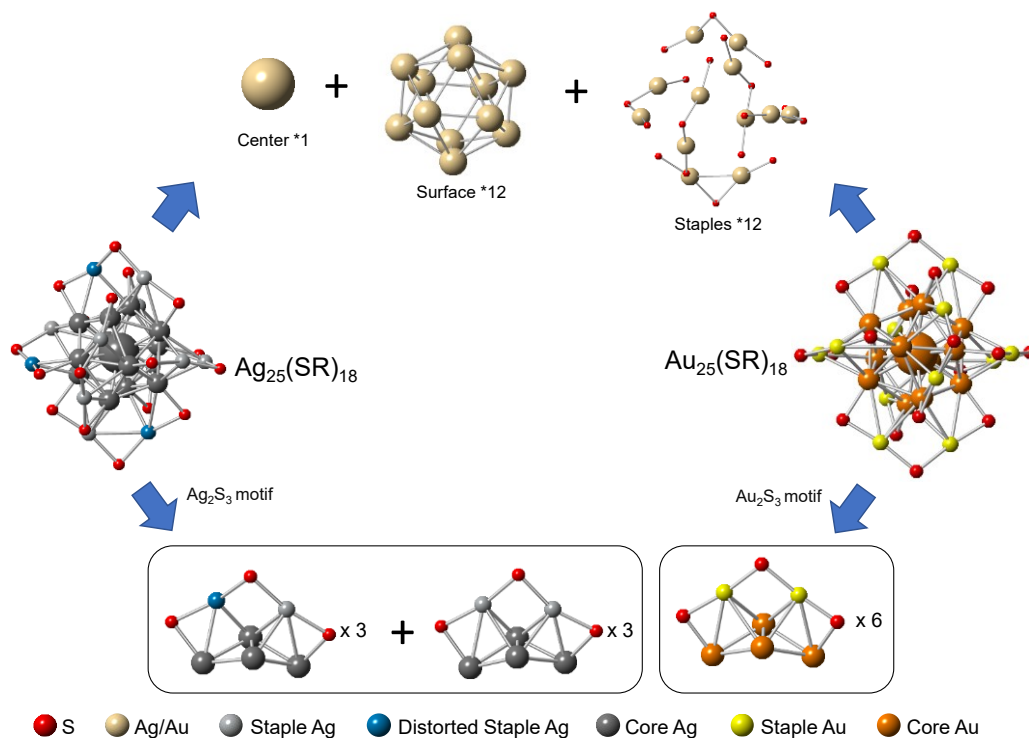


**Figure A1.** Crystal structure of  $\text{Ag}_{25}(\text{SR})_{18}$  and  $\text{Au}_{25}(\text{SR})_{18}$  with illustration of their differences and similarity. Carbon and hydrogen atoms in ligands are not shown for clarity.

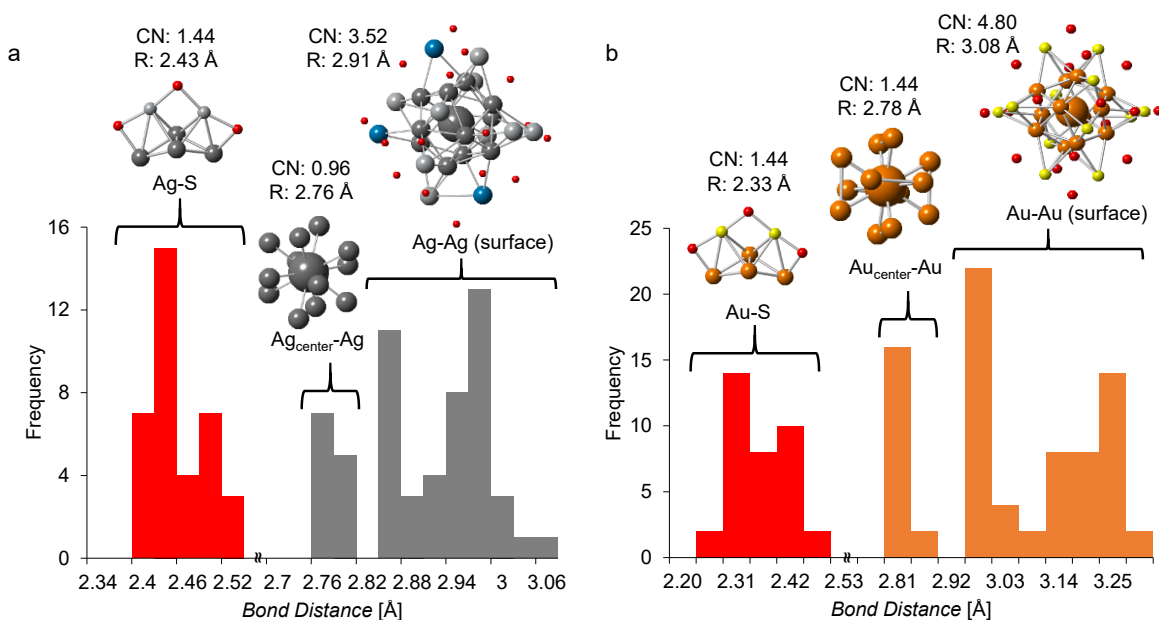









**Figure A2.** Comparison of the bond distribution of a)  $\text{Ag}_{25}$  and b)  $\text{Au}_{25}$ .

# Appendix B – Copyright Agreement for Chapter 1

7/6/2020

Rightslink® by Copyright Clearance Center

 **Copyright Clearance Center**  **RightsLink®**  Home  Help  Email Support  Sign in  Create Account

## Impact of Protecting Ligands on Surface Structure and Antibacterial Activity of Silver Nanoparticles



Author: J. Daniel Padmos, Robert T. M. Boudreau, Donald F. Weaver, et al

Publication: Langmuir

Publisher: American Chemical Society

Date: Mar 1, 2015

Copyright © 2015, American Chemical Society

### PERMISSION/LICENSE IS GRANTED FOR YOUR ORDER AT NO CHARGE

This type of permission/license, instead of the standard Terms & Conditions, is sent to you because no fee is being charged for your order. Please note the following:

- Permission is granted for your request in both print and electronic formats, and translations.
  - If figures and/or tables were requested, they may be adapted or used in part.
  - Please print this page for your records and send a copy of it to your publisher/graduate school.
  - Appropriate credit for the requested material should be given as follows: "Reprinted (adapted) with permission from (COMPLETE REFERENCE CITATION). Copyright (YEAR) American Chemical Society." Insert appropriate information in place of the capitalized words.
  - One-time permission is granted only for the use specified in your request. No additional uses are granted (such as derivative works or other editions). For any other uses, please submit a new request.
- If credit is given to another source for the material you requested, permission must be obtained from that source.

[BACK](#)

[CLOSE WINDOW](#)

© 2020 Copyright - All Rights Reserved | [Copyright Clearance Center, Inc.](#) | [Privacy statement](#) | [Terms and Conditions](#)  
Comments? We would like to hear from you. E-mail us at [customer-care@copyright.com](mailto:customer-care@copyright.com)

## Appendix C – Copyright Agreements for Chapter 2

7/14/2020

RightsLink - Your Account

### JOHN WILEY AND SONS LICENSE TERMS AND CONDITIONS

Jul 14, 2020

This Agreement between Ziyi Chen ("You") and John Wiley and Sons ("John Wiley and Sons") consists of your license details and the terms and conditions provided by John Wiley and Sons and Copyright Clearance Center.

License Number	4867811055059
License date	Jul 14, 2020
Licensed Content Publisher	John Wiley and Sons
Licensed Content Publication	Advanced Materials
Licensed Content Title	Single-Atom Catalysts Supported by Crystalline Porous Materials: Views from the Inside
Licensed Content Author	Tianjun Zhang, Ziyi Chen, Andrew G. Walsh, et al
Licensed Content Date	Jul 12, 2020
Licensed Content Volume	0
Licensed Content Issue	0
Licensed Content Pages	29
Type of Use	Dissertation/Thesis
Requestor type	Author of this Wiley article
Format	Print and electronic
Portion	Text extract
Number of Pages	2
Will you be translating?	No
Title	X-ray Spectroscopy Studies of Ligand-protected and Zeolite-confined Silver Nanoclusters
Institution name	Dalhousie University
Expected presentation date	Aug 2020
Portions	Part of Section 2.1, Figure 1
Requestor Location	Ziyi Chen 5264 Morris Street  Halifax, NS B3J 1B5 Canada Attn: Ziyi Chen
Publisher Tax ID	EU826007151
Total	<b>0.00 CAD</b>
Terms and Conditions	

#### TERMS AND CONDITIONS

This copyrighted material is owned by or exclusively licensed to John Wiley & Sons, Inc. or one of its group companies (each a "Wiley Company") or handled on behalf of a society with which a Wiley Company has exclusive publishing rights in relation to a particular work (collectively "WILEY"). By clicking "accept" in connection with completing this licensing transaction, you agree that the following terms and conditions apply to this transaction (along with the billing and payment terms and conditions established by the Copyright Clearance Center Inc., ("CCC's Billing and Payment terms and conditions"), at the time that you opened your RightsLink account (these are available at any time at <http://myaccount.copyright.com>).

#### Terms and Conditions

- The materials you have requested permission to reproduce or reuse (the "Wiley Materials") are protected by copyright.

<https://s100.copyright.com/MyAccount/web/jsp/viewprintablelicensefrommyorders.jsp?ref=a85291f4-400a-4e0f-ade4-c19a7d56ce7b&email=>

1/4



RightsLink®



Home



Help



Email Support



Sign in



Create Account

### X-ray Spectroscopy of Gold-Thiolate Nanoclusters

Author: Peng Zhang

Publication: The Journal of Physical Chemistry C

Publisher: American Chemical Society

Date: Nov 1, 2014

Copyright © 2014, American Chemical Society



ACS Publications  
Most Trusted. Most Cited. Most Read.

#### PERMISSION/LICENSE IS GRANTED FOR YOUR ORDER AT NO CHARGE

This type of permission/license, instead of the standard Terms & Conditions, is sent to you because no fee is being charged for your order. Please note the following:

- Permission is granted for your request in both print and electronic formats, and translations.
  - If figures and/or tables were requested, they may be adapted or used in part.
  - Please print this page for your records and send a copy of it to your publisher/graduate school.
  - Appropriate credit for the requested material should be given as follows: "Reprinted (adapted) with permission from (COMPLETE REFERENCE CITATION). Copyright (YEAR) American Chemical Society." Insert appropriate information in place of the capitalized words.
  - One-time permission is granted only for the use specified in your request. No additional uses are granted (such as derivative works or other editions). For any other uses, please submit a new request.
- If credit is given to another source for the material you requested, permission must be obtained from that source.

[BACK](#)

[CLOSE WINDOW](#)



RightsLink®



Home



Help



Email Support



Sign in



Create Account

**Structure of Tiopronin-Protected Silver Nanoclusters in a One-Dimensional Assembly**

Author: J. Daniel Padmos, Robert T. M. Boudreau, Donald F. Weaver, et al

Publication: The Journal of Physical Chemistry C

Publisher: American Chemical Society

Date: Oct 1, 2015

*Copyright © 2015, American Chemical Society***PERMISSION/LICENSE IS GRANTED FOR YOUR ORDER AT NO CHARGE**

This type of permission/license, instead of the standard Terms & Conditions, is sent to you because no fee is being charged for your order. Please note the following:

- Permission is granted for your request in both print and electronic formats, and translations.
  - If figures and/or tables were requested, they may be adapted or used in part.
  - Please print this page for your records and send a copy of it to your publisher/graduate school.
  - Appropriate credit for the requested material should be given as follows: "Reprinted (adapted) with permission from (COMPLETE REFERENCE CITATION). Copyright (YEAR) American Chemical Society." Insert appropriate information in place of the capitalized words.
  - One-time permission is granted only for the use specified in your request. No additional uses are granted (such as derivative works or other editions). For any other uses, please submit a new request.
- If credit is given to another source for the material you requested, permission must be obtained from that source.

[BACK](#)[CLOSE WINDOW](#)